Analytic and Numerical Approaches to Radiation and Transmission of EM Waves in

Lossy Media

by

Sai Zhou

A Dissertation Presented in Partial Fulfillment
of the Requirements for the Degree
Doctor of Philosophy

Approved November 2021 by the
Graduate Supervisory Committee:

George Pan, Chair
James Aberle
David Allee
Joseph Palais

ARIZONA STATE UNIVERSITY

December 2021

ABSTRACT

This dissertation consists of four parts: design of antenna in lossy media, analysis of wire antennas using electric field integral equation (EFIE) and wavelets, modeling and measurement of grounded waveguide coplanar waveguide (GCPW) for automotive radar, and E-Band 3-D printed antenna and measurement using VNA. In the first part, the antenna is modeled and simulated in lossy media. First, the vector wave functions is solved in the fundamental mode. Next the energy flow velocity is plotted to show near-field energy distribution for both TM and TE in air and seawater environment. Finally the power relation in seawater is derived to calculate the source dipole moment and required power.

In the second part, the current distribution on the antenna is derived by solving EFIE with moment of methods (MoM). Both triangle and Coifman wavelet (Coiflet) are used as basis and weight functions. Then Input impedance of the antenna is computed and results are compared with traditional sinusoid current distribution assumption. Finally the input impedance of designed antenna is computed and matching network is designed and show resonant at designed frequency.

In the third part, GCPW is modeled and measured in E-band. Laboratory measurements are conducted in 75 to 84 GHz. The original system is embedded with error boxes due to misalignment and needed to be de-embedded. Then the measurement data is processed and the results is compared with raw data.

In the fourth part, the horn antennas and slotted waveguide array antenna (SWA) are designed for automotive radar in 75GHz to 78GHz. The horn antennas are fabricated using 3D printing of ABS material, and electro-plating with copper. The analytic solution and HFSS simulation show good agreement with measurement.

TABLE OF CONTENTS

ii

LIST OF TABLES

LIST OF FIGURES

Chapter 1

DESIGN OF ANTENNA IN LOSSY MEDIUM

1.1 Introduction

Based upon spherical harmonics, L. J. Chu published a historic paper [1] on the fundamental limits for electrically small antennas, which is known as the Chu-Fano theorem and it laid the foundation for small antennas in free-space at relatively low frequencies. Over the past half century, Wheeler, Harrington, Collin, et al. have extended and elaborated the Chu-Fano criterion [2]–[4]. The physical bounds of gain and Q-factor of linearly polarized antennas is well studied and presented in [5]. Current distribution in conducting medium can be approximated by integral equation [6], [7]. Propagation behavior of electromagnetic (EM) waves in lossy medium have been studied using Hertzian potential integrals and dispersion relation [8]–[10]. Recently, commercial and scientific interests have moved upward toward higher frequencies in microwave, millimeter wave, and optical regions [11]–[16], due to internet and wireless communication advancement. Nonetheless, low frequency EM signals can penetrate through conductive medium such as human tissue, seawater, soil, rock, and building materials. As a result, the study of small dipoles in conducting medium is inspired by ground penetrating radar, underground water, and biomedical applications, e.g., artificial cardiac pacemaker [17].

In 2017, Troy Olsson launched a DARPA project, A MEchanically Based Antenna (AMEBA), to penetrate RF requirements with an antenna system that has the highest theoretical efficiency possible, and minimize Ohmic losses which are intrinsic due to

the lossy environment. The targeted RF carrier frequencies are less than 30 kHz, and the goal is to achieve a low-size, weight, and power (SWaP) man-portable system: Deliver sufficient magnetic field strength for low data rate communications at relevant distances, and efficiently modulate the RF carrier at useful data rates. The research project in this chapter was motivated by the DARPA AMEBA [18].

First begin with review of vector wave functions and identified that the Hertz dipole in free-space in a special case of TE10, lowest radiation mode. The Hertzian electric dipole equations in free-space [19], [20]. Then the model is extended to electrically lossy medium in both frequency and time domain. Both electric and magnetic dipoles are studied in air and lossy seawater environment with no passive structure. Numerical results show that such an extension is valid and accurate for electric dipoles of large gap dimension and fat wire diameters. For electric small antennas, the reactive power in near field is dominant and significant to device functionality [21]. In time-domain, the radial energy flow velocity is calculated at specific time to compare the reactive energy in air and lossy medium. For EM waves in ELF and VLF bands, the free-space wavelengths range from tens to thousands of kilometers, resulting in extremely small $|ka|$, where k is the wavenumber and a is one half of the dipole length. Our analytical model reveals that in electrically lossy medium the radiation efficiency for electrically small antennas is proportional to $|ka|^3$ for TM (electric) and $|ka|$ for TE (magnetic) radiator, making magnetic antennas more efficient than electric ones over two to three orders of magnitude.

In the chapter, more attention is paid to the magnetic dipole because of its better performance and rear appearance in the literature. Magnetic current based antennas (MCA) are less popular than electric counterparters by far [22]–[26]. The contra-wound toroidal helix antenna (CTHA) was studied numerically and experimentally at

the VHF band [23], [24]. Studies reported there were for CTHA with air core without electrets. The CTHA is a low-profile low-directivity surface-mounted antenna with reasonable efficiency at a height of less than $\lambda/30$. It operates at the inductive side of resonance, so that it can be tuned with a high-efficiency capacitor. McDonald has published a series MCA papers in tensor forms [25]. The near zone field analyses of MCA were also reported for physical therapy [27]. Magnetic antennas with dielectric core or ferromagnetic laminate composite materials are referred to as permeable antenna [28].

Another option to achieve a low-size, weight, and power (SWaP) man-portable system is the dipole due to mechanically spinning of an electret or magnet, which is smaller in size and weight compared to its electromagnetic counterpartners. However, it requires more power to maintain the rotation and a flywheel is required [29].

Under seawater sensing and communication are dominated by sonar via acoustic waves because seawater is too lossy for RF signals. However, acoustic signals cannot communicate with a satellite in space or a radio station in land. If electromagnetic (EM) waves are used for under seawater, the frequency must be very low, because skin depth δ (measure of penetration of EM waves in conducting medium) is inversely proportional to $\sqrt{f}$. This chapter investigates simple, compact, and low-power methods for generating extremely low-frequency (ULF-VLF) radio signals in 300 Hz to 30 KHz in lossy medium. The topic of this chapter is motivated by the prohibitively large size and low efficiency of conventional antennas operating in this frequency range. Studies of generating electromagnetic waves by mechanically rotating magnets and electrets are conducted, which has been experimentally implemented in many other papers [30], [31].

| (a) | (b) | (c) |
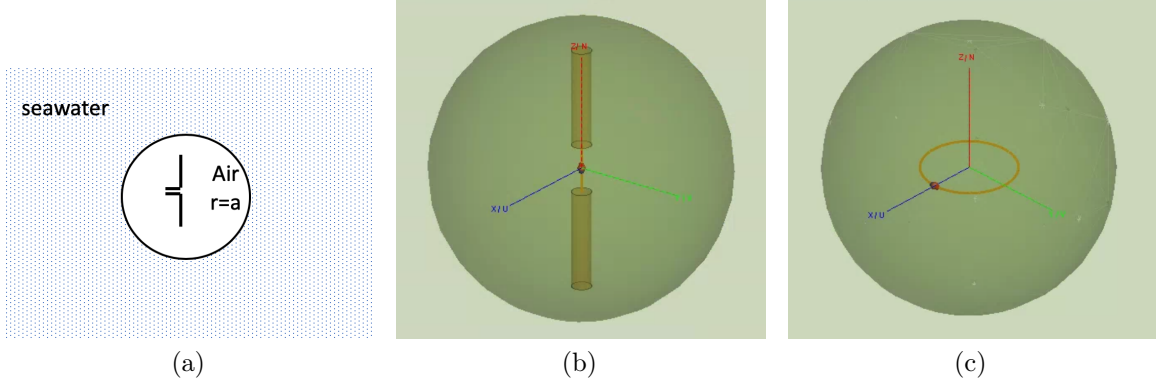
Figure 1. Dipole antenna surrounded by seawater. (a) Configuration of small dipole. (b) Feko model of TM antenna. (c) Feko model of TE antenna

1.2 Review of Vector Wave Functions

Within any source-free, homogeneous, and isotropic medium, the characteristic solution to vector wave equation in spherical coordinate is [19]

$$\psi_{nm} = {\textstyle{\cos \atop \sin}}(m\phi)P_n^m(\cos\theta)z_n(kr) \tag{1.1}$$

where time-dependency $e^{j\omega t}$ is suppressed throughout is assumed,

$$k^2 = \epsilon\mu\omega^2 - j\sigma\mu\omega \tag{1.2}$$

$P_n^m(\cos\theta)$ is associated Legendre polynomials, and $z_n(kr)$ is spherical Bessel function with four possible forms

$$j_n(kr), \text{standing wave} \tag{1.3}$$

$$y_n(kr), \text{standing wave} \tag{1.4}$$

$$h_n^{(1)}(kr), \text{incoming wave} \tag{1.5}$$

$$h_n^{(2)}(kr), \text{outgoing wave} \tag{1.6}$$

Use (1.6) for the radiation fields for $r > a$. In region $r < a$, use (1.3) since the field is finite at the origin. Then boundary condition may be used to determine the field.

Next use the scalar function ψ_{nm} to construct three set of independent vector wave equation solutions $\vec{L}_{nm}$, $\vec{M}_{nm}$, $\vec{N}_{nm}$

$$\vec{L} = \nabla\psi = \frac{\partial\psi}{\partial r}\hat{r} + \frac{1}{r}\frac{\partial\psi}{\partial\theta}\hat{\theta} + \frac{1}{r\sin\theta}\frac{\partial\psi}{\partial\phi}\hat{\phi} \qquad (1.7)$$

$$\vec{M} = \nabla \times \vec{\alpha}\psi \qquad (1.8)$$

$$\vec{N} = \frac{1}{k}\nabla \times \vec{M} \qquad (1.9)$$

where $\vec{\alpha}$ is a constant vector. Next substitute (1.1) to (1.7),

$$\vec{L}_{nm} = {}^{\cos}_{\sin}(m\phi)P_n^m(\cos\theta)\frac{\partial}{\partial r}z_n(kr)\hat{r}+$$
$$\frac{1}{r}{}^{\cos}_{\sin}(m\phi)\frac{\partial}{\partial\theta}P_n^m(\cos\theta)z_n(kr)\hat{\theta}\mp$$
$$\frac{m}{r\sin\theta}\frac{\partial}{\partial\phi}{}^{\sin}_{\cos}(m\phi)P_n^m(\cos\theta)z_n(kr)\phi \qquad (1.10)$$

Since the medium is source free, electromagnetic fields $\vec{E}$ and $\vec{H}$ can be represented as linear combination of solenoidal solutions $\vec{M}$ and $\vec{N}$ as

$$\vec{E}(r,\theta,\phi) = \sum_{n=0}^{\infty}\sum_{m=-n}^{n}[a_{nm}\vec{M}_{nm} + b_{nm}\vec{N}_{nm}] \qquad (1.11)$$

$$\vec{H}(r,\theta,\phi) = \frac{1}{j\eta}\sum_{n=0}^{\infty}\sum_{m=-n}^{n}[a_{nm}\vec{N}_{nm} + b_{nm}\vec{M}_{nm}] \qquad (1.12)$$

To find the independent solutions $\vec{M}$ and $\vec{N}$, let $\vec{\alpha} = r\hat{r}$ then $\vec{M}$ is tangential to the sphere surface. After some mathematic derivation

$$\vec{M}_{nm} = \frac{1}{\sin\theta}\frac{\partial}{\partial\phi}(\psi)\hat{\theta} - \frac{\partial}{\partial\theta}(\psi)\hat{\phi}$$
$$= \mp\frac{m}{\sin\theta}{}^{\sin}_{\cos}(m\phi)P_n^m(\cos\theta)z_n(kr)\hat{\theta}-$$
$${}^{\cos}_{\sin}(m\phi)\frac{\partial}{\partial\theta}P_n^m(\cos\theta)z_n(kr)\hat{\phi} \qquad (1.13)$$

5

Then

$$\vec{N}_{nm} = \frac{1}{k}\nabla \times \vec{M}_{nm}$$

$$= \frac{n(n+1)}{kr}\psi\hat{r} + \frac{1}{kr}\frac{\partial^2}{\partial r\partial\theta}(r\psi)\hat{\theta} + \frac{1}{kr\sin\theta}\frac{\partial^2}{\partial r\partial\phi}(r\psi)\hat{\phi}$$

$$= \frac{n(n+1)}{kr}{}^{\cos}_{\sin}(m\phi)P_n^m(\cos\theta)z_n(kr)\hat{r}+$$

$$\frac{1}{kr}{}^{\cos}_{\sin}(m\phi)\frac{\partial}{\partial\theta}P_n^m(\cos\theta)\frac{\partial}{\partial r}[rz_n(kr)]\hat{\theta}\mp$$

$$\frac{m}{kr\sin\theta}{}^{\sin}_{\cos}(m\phi)P_n^m(\cos\theta)\frac{\partial}{\partial r}[rz_n(kr)]\hat{\phi} \tag{1.14}$$

For the fundamental mode, $n = 1, m = 0$, $\vec{m}_{nm}$ and $\vec{n}_{nm}$ reduce to

$$\vec{M}_{10} = -\frac{1}{k}\left(\frac{1}{r} + \frac{1}{jkr^2}\right)\sin\theta\hat{\phi} \tag{1.15}$$

$$\vec{N}_{10} = \frac{1}{k}\left(\frac{1}{r} + \frac{1}{jkr^2} - \frac{1}{k^2r^3}\right)\sin\theta\hat{\theta}-$$

$$\frac{2}{k}\left(\frac{1}{kr^2} + \frac{1}{jk^2r^3}\right)\cos\theta\hat{r} \tag{1.16}$$

1.3   Electromagnetic fields due to electric- and magnetic- dipoles

This dissertation use the SI unit system, and time convention of $e^{j\omega t}$ is assumed and suppressed. Under the lowest mode assumption, the field components of electric dipole (TM antenna) are [20]

$$H_\phi = \frac{I_e dl}{4\pi}jke^{-jkr}\left(\frac{1}{r} + \frac{1}{jkr^2}\right)\sin\theta$$

$$E_\theta = \eta\frac{I_e dl}{4\pi}jke^{-jkr}\left(\frac{1}{r} + \frac{1}{jkr^2} - \frac{1}{k^2r^3}\right)\sin\theta \tag{1.17}$$

$$E_r = \eta\frac{I_e dl}{4\pi}jke^{-jkr}\left(\frac{2}{jkr^2} - \frac{2}{k^2r^3}\right)\cos\theta$$

where dl is dipole length, or $dl = 2a$. The equations ware derived for lossless environment; wavenumber $k = \omega\sqrt{\mu\varepsilon}$ is real, wave impedance $\eta = \sqrt{\mu/\varepsilon}$, I_e is electric current.

By duality, for magnetic dipole (TE antenna):

$$E_\phi = -\frac{I_m dl}{4\pi} k e^{-\mathrm{j}kr} \left(\frac{1}{r} + \frac{1}{\mathrm{j}kr^2} \right) \sin\theta$$

$$H_\theta = \frac{1}{\eta} \frac{I_m dl}{4\pi} k e^{-\mathrm{j}kr} \left(\frac{1}{r} + \frac{1}{\mathrm{j}kr^2} - \frac{1}{k^2 r^3} \right) \sin\theta \qquad (1.18)$$

$$H_r = \frac{1}{\eta} \frac{I_m dl}{4\pi} k e^{-\mathrm{j}kr} \left(\frac{2}{\mathrm{j}kr^2} - \frac{2}{k^2 r^3} \right) \cos\theta$$

where I_m is magnetic current. As shown in Fig. 1 (a), the antenna is inside air-filled sphere of radius $a = 0.3$ m and surrounded by seawater and operating at $f = 1000$ Hz. The parameters of $a = 0.3$ m, $f = 1$ kHz will be assumed through out the entire chapter.

Extend (1.17) and (1.18) to more general cases below: (a) Air or free-space with $k = k_0$, (b) Lossy medium with complex permittivity, and (c) Seawater (highly lossy).

1.3.1 In air environment (Lossless)

In equations (1.17) and (1.18), use $k = k_0 = \omega/c = 2.094 \times 10^{-5} \mathrm{m}^{-1}$, wavelength $\lambda = \lambda_0 = c/f = 3 \times 10^5 \mathrm{m}$, wave impedance $\eta_0 = 377\Omega$. The magnitude ratio of the normalized E- to H-field as a function of normalized distance r/λ is plotted in Fig. 2 (a). The far-zone field components are those proportional to the $1/r$ term in Eq. (1.17) and (1.18). It is seen that the far-zone can be considered when distance $r \geq 1.0\lambda$. It is obvious that in the far-zone $|E/H|_{\mathrm{TM}} = |E/H|_{\mathrm{TE}} = \eta_0 = 377\Omega$, free-space intrinsic impedance, which is the asymptotic value as $r \to \infty$. On the contrary, the two ratios in the near zone have opposite trends when distance shrinks toward zero, as seen in Fig. 2 (a). When distance $r \to 0$, impedance curve grows rapidly for electric dipole, while the other curve fast decreases for magnetic dipole. Fig. 2 (a) is identical to the plot in [25] which was derived in the Gaussian CGS units.
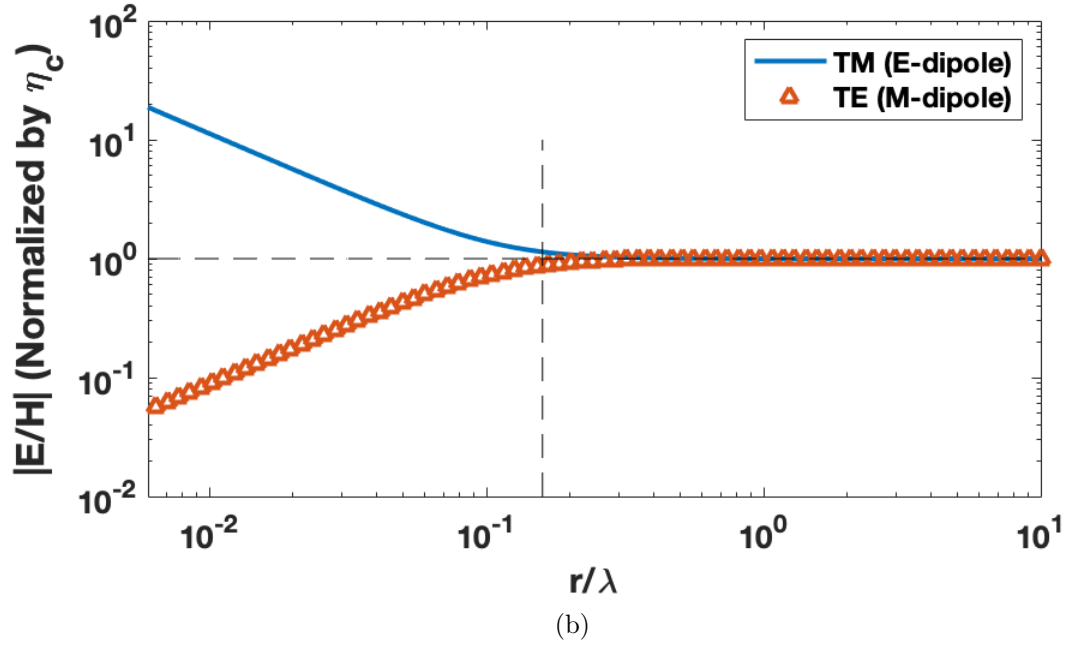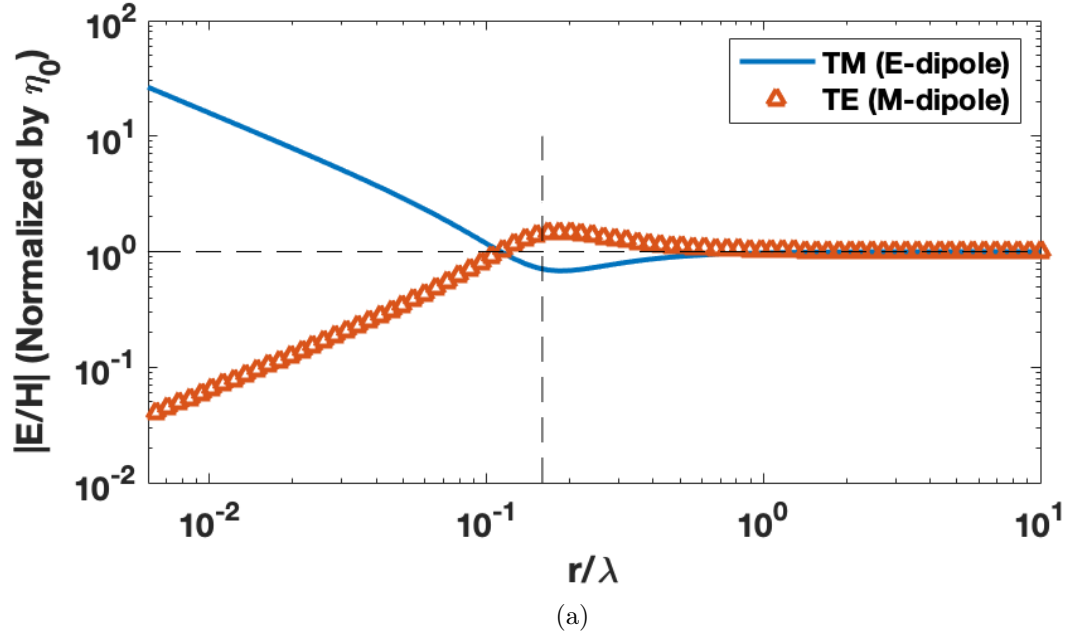
Figure 2. Normalized impedance versus distance for E-dipole and H-dipole in: (a) air and (b) seawater

1.3.2 Lossy Medium (Complex permittivity)

In a lossy medium of relative permittivity ε_r and conductivity σ, the complex permittivity $\varepsilon = \varepsilon_c = \varepsilon_0 \left(\varepsilon_r - j\frac{\sigma}{\omega \varepsilon_0} \right) = \varepsilon' - j\sigma/\omega$, complex wavenumber $k = \omega\sqrt{\mu \varepsilon_c}$, complex propagation constant $\gamma := \alpha + j\beta = jk$, and complex wave impedance $\eta_c = \eta_0 \omega (\beta + j\alpha)/(|k|^2 c)$.

Using complex valued $k = \beta - j\alpha$ and $\eta = \eta_c$ in (1.17) and (1.18), the average power outflows, passing a fictitious sphere of radius r for the electric and magnetic-dipole, are respectively

$$
\begin{aligned}
S_{\text{TM}}(r) =& \frac{1}{2}\text{Re} \oint \vec{E} \times \vec{H}^* \cdot \vec{n}ds \\
=& \frac{1}{12\pi} (I_e dl)^2 \frac{\eta_0 \omega}{c} e^{-2\alpha r} \beta \times \\
& \left[1 + \frac{2\alpha}{|k|^2 r} + \frac{1}{|k|^2 r^2} - \frac{\beta^2 - 3\alpha^2}{|k|^4 r^2} + \frac{2\alpha}{|k|^4 r^3} \right]
\end{aligned} \tag{1.19}
$$

$$
S_{\text{TE}}(r) = \frac{1}{12\pi} (I_m dl |k|)^2 \frac{c}{\eta_0 \omega} e^{-2\alpha r} \beta \left[1 + \frac{2\alpha}{|k|^2 r} \right] \tag{1.20}
$$

The detail of above derivation is presented in Appendix A.

1.3.3 In seawater environment (Highly Lossy, $\sigma \gg \omega \varepsilon_0 \varepsilon_r$)

For highly lossy seawater, conductivity $\sigma = 4$ S/m and relative permittivity $\varepsilon_r = 80$. Thus, complex permittivity, $\varepsilon_c = \varepsilon_0 \left(80 - j\frac{4}{2\pi \times 10^3 \times 8.854 \times 10^{-12}} \right) = \varepsilon_0 (80 - j7.19 \times 10^7)$, complex wavenumber $k = \frac{\omega}{c}\sqrt{80 - j7.19 \times 10^7} \approx 0.1256(1 - j) = \beta - j\alpha$, showing $\alpha = \beta \approx 0.1256$ m^{-1}. The skin depth, $\delta = 1/\alpha = 7.96$m ≈ 8m, wavelength, $\lambda = 2\pi/\beta = 50.0341$m ≈ 50m at frequency $f = 1$ kHz, complex propagation constant $\gamma = jk = 0.1256(1 + j)$m^{-1}, and $\eta_c = \sqrt{\mu_0/\varepsilon_c} \approx 0.0314(1 + j)\Omega$. The

magnitude ratio of the E-field to H-field is plotted in Fig. 2 (b), where the far-zone field components are those proportional to the $1/r$ terms in (1.17) and (1.18). It is obvious that far-zone can be considered when distance $r \geq 1.0\lambda$. In the far-zone $|E/H|_{\mathrm{TM}} = |E/H|_{\mathrm{TE}} = |\eta_c| = 0.0444\Omega$, independent of r. On the contrary, as $r \to 0$, the two ratios in the near field zone have opposite trends, as seen in Fig. 2 (b). Contrary to Fig. 2 (a), the two impedance curves are monotonically varying with distance in lossy environment.

1.3.4 Numerical Verification

Using commercial software, Feko, to conduct the simulation. A small E-dipole is centered in a hollow sphere of $r = 0.3$m, which is submerged in a seawater sphere of outer radius $R = 400$m. Seawater conductivity $\sigma = 4$S/m and relative permittivity $\varepsilon_r = 80$, rendering $\gamma = \mathrm{j}k = 0.1256(1 + \mathrm{j})\mathrm{m}^{-1}$, $\alpha = \beta \approx 0.1256\mathrm{m}^{-1}$. Depicted in Fig. 1 (b) is a TM antenna with conducting rod of radius $\rho = 0.02$m, length $\ell = 0.2$m for each arm, and gap $g = 0.1$m in the middle for source excitation. This fat dipole with large gap is deliberately exaggerated to test the validity of analytic model of Eqs. (1.17) and (1.18) in lossy environment. Figure 1 (c) illustrates the Feko model of a TE antenna with loop radius 0.1m, wire radius 0.1mm. Again, the TE antenna is contained in an air-filled sphere of $r = 0.3$m, which is submerged in seawater. The Feko evaluated total E-field and H-field at various distances from the antenna are compared with analytic solutions in Fig. 3 and excellent agreement is observed. The $L2$ errors are 0.31% for TM and 0.12% for TE.
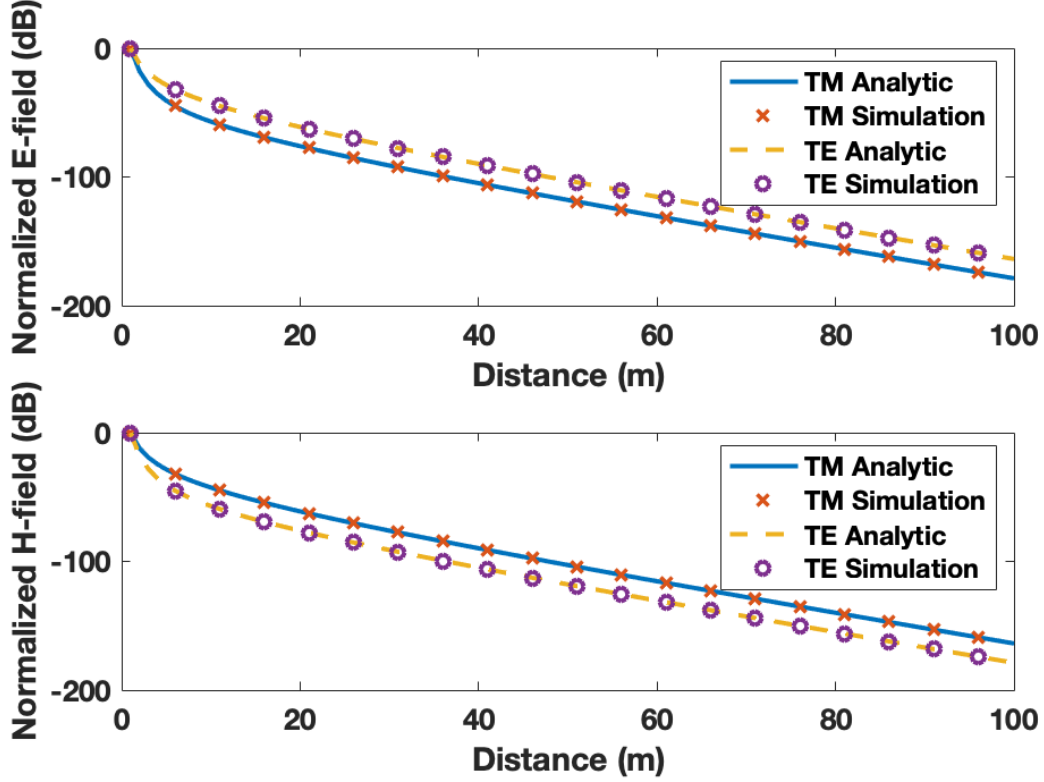
Figure 3. Comparison of E- and H-field between analytic solution with simulation results for TM and TE dipole antennas

1.4 Energy Flow Velocity in Time Domain

The main purpose of the underwater antenna is to conduct short-range communication, and EFV is an important quantity in studying the reactive energy in the near-field of an antenna [21]. This section will study antenna's EFV in both free space and lossy seawater.

The electromagnetic energy flow velocity is, $\boldsymbol{v} = \boldsymbol{S}/w$, where $\boldsymbol{S} = \boldsymbol{E} \times \boldsymbol{H}$ is the Poynting vector and $w = \frac{1}{2}\varepsilon|\boldsymbol{E}|^2 + \frac{1}{2}\mu|\boldsymbol{H}|^2$ is the stored electromagnetic energy.

1.4.1 Lossless Medium

The time-domain electromagnetic fields of TM antenna in free space can be found in [32]

$$E_\theta(t,r,\theta) = \frac{\eta dl}{4\pi r}\left[\frac{1}{c}\frac{d}{dt}i\left(t-\frac{r}{c}\right) + \frac{1}{r}i\left(t-\frac{r}{c}\right) + \right.$$
$$\left. \frac{c}{r^2}\int_{-\infty}^{t} i\left(\tau-\frac{r}{c}\right)d\tau\right]\sin\theta \tag{1.21}$$

$$E_r(t,r,\theta) = \frac{\eta dl}{2\pi r^2}\left[i\left(t-\frac{r}{c}\right) + \frac{c}{r}\int_{-\infty}^{t} i\left(\tau-\frac{r}{c}\right)d\tau\right]\cos\theta \tag{1.22}$$

$$H_\phi(t,r,\theta) = \frac{dl}{4\pi r}\left[\frac{1}{c}\frac{d}{dt}i\left(t-\frac{r}{c}\right) + \frac{1}{r}i\left(t-\frac{r}{c}\right)\right]\sin\theta \tag{1.23}$$

Similarly, for TE case

$$H_\theta(t,r,\theta) = \frac{1}{\eta}\frac{dl}{4\pi r}\left[\frac{1}{c}\frac{d}{dt}i\left(t-\frac{r}{c}\right) + \frac{1}{r}i\left(t-\frac{r}{c}\right) + \right.$$
$$\left. \frac{c}{r^2}\int_{-\infty}^{t} i\left(\tau-\frac{r}{c}\right)d\tau\right]\sin\theta \tag{1.24}$$

$$H_r(t,r,\theta) = \frac{1}{\eta}\frac{dl}{2\pi r^2}\left[i\left(t-\frac{r}{c}\right) + \frac{c}{r}\int_{-\infty}^{t} i\left(\tau-\frac{r}{c}\right)d\tau\right]\cos\theta \tag{1.25}$$

$$E_\phi(t,r,\theta) = \frac{dl}{4\pi r}\left[\frac{1}{c}\frac{d}{dt}i\left(t-\frac{r}{c}\right) + \frac{1}{r}i\left(t-\frac{r}{c}\right)\right]\sin\theta \tag{1.26}$$

By using time dependent current source, $i(t) = i_0\sin(\omega_0 t)u(t)$, where $u(t)$ is the unit step function which is turned on at $t = 0$.

In free space (or lossless medium), the time-domain normalized radial EFV within one wavelength is shown in Fig. 4 (a) and (b) for TE and TM respectively. Our TM result of Fig. 4 (a) repeated the pattern in [32]. EFV is highly related to radiation efficiency. For TE antenna in lossless medium, Fig. 4 (b), its EFV is identical to TM EFV because both of them has efficiency of 100%. And both patterns are showing as orange lobes. When displaying the process in real time video, the patterns behave

like creation of soap bubbles: detaching from the dipole body and growing along the radius direction.
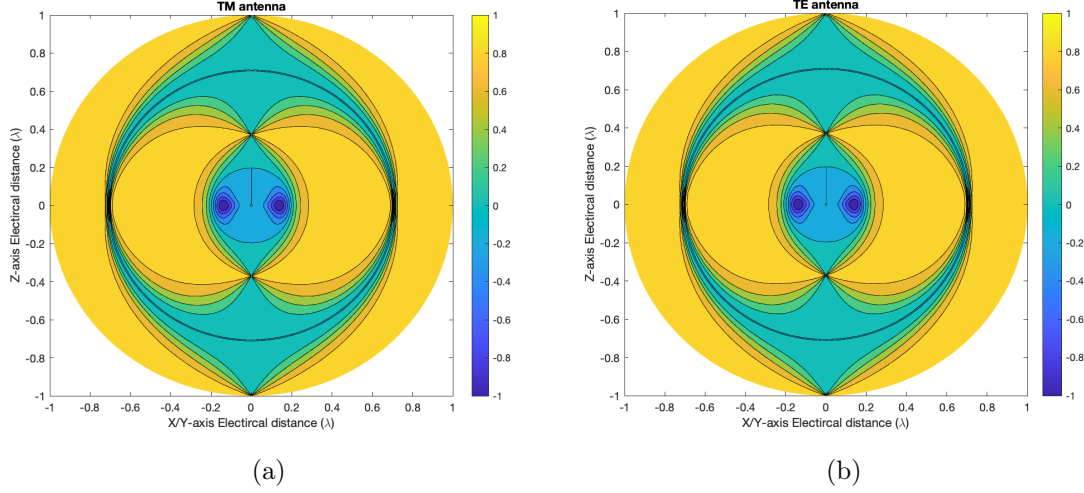
Figure 4. Normalized radial energy flow velocity (v_r/c) at $t = 2T_0$ in lossless medium. (a) TM antenna. (b) TE antenna.

1.4.2 Lossy Medium

In a lossy medium, e.g., seawater, substitute complex permittivity into equations (1.21)-(1.23) and (1.24)-(1.26). assume the conductivity $\sigma = 4$ S/m and relative permittivity $\varepsilon_r = 80$, wavelength becomes $\lambda = 50.0341$m, speed of light $c_{\text{water}} \approx 50$km/s. The results are shown in Fig. 5.

On the contrary, Fig. 5 (a) and (b) illustrate the EFVs for TE and TM dipoles in highly lossy seawater. They clearly demonstrate that the radial EFV of TE dipole is mainly in the radiation mode (showing as orange lobes), while TM dipole is essentially in cavity mode (showing as onion layers). Time-domain quantities are highly intriguing,
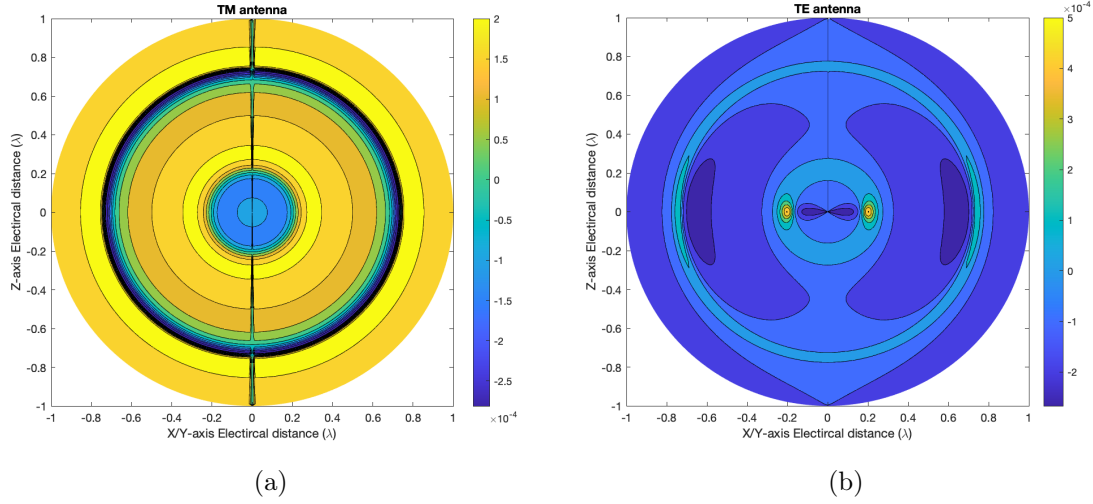
Figure 5. Normalized radial energy flow velocity (v_r/c) at $t = 2T_0$ in lossy medium. (a) TM antenna. (b) TE antenna.

and here it shows why radiation efficiency for TE is much better than TM from a qualitative and intuitive point of view. The super radiation efficiency of the TE over TM in a lossy medium is revealed by EFV pattern in time-domain. Figure 5 (b) of TE dipole in lossy medium indicates that radiation EFV pattern is like orange lobes, while Fig. 5 (a) of TM dipole pattern looks like onion layers. When displaying the process in real time video, Fig. 5 (b) behaves like creation of soap bubbles, similar to Fig. 4. In contrast, the corresponding time domain video of Fig. 5 (a) shows standing wave pattern of concentric face-to-face hemi-balloons.

1.5 Power Relation in Seawater

Low frequency propagation of EM wave in conducting medium plays an important role in low data rate communication under seawater. In highly lossy seawater, source generated power is mostly dissipated in near-zone region for electrically small antennas

Table 1. Numerical values at $r = 0.3$m, near-zone

$\frac{2\alpha}{|k|^2 r}$	$\frac{1}{|k|^2 r^2}$	$\frac{\beta^2 - 3\alpha^2}{|k|^4 r^2}$	$\frac{2\alpha}{|k|^4 r^3}$
26.5439	352.2895	-352.2887	9.3511e+3

of $\ell \ll \lambda$. This section will derive a closed form expression of Ohmic loss in a lossy sphere, and use it to study radiation efficiency of small electric and magnetic dipoles.

The power outflow consists of radiated power and Ohmic losses. Setting $\alpha = 0 \Rightarrow \beta = k$, the general power equations of (1.19) and (1.20) reduce to lossless case; Meanwhile, both square brackets in (1.19) and (1.20) reduce to unity, meaning the net power flow is the radiated power. Therefore, term 1 in the brackets of (1.19) and (1.20) is the radiated power, while other higher-order terms represent power loss due to the evanescent fields.

For high lossy medium, e.g., seawater, $|k| = \sqrt{2}\alpha = \sqrt{2}\beta$, which reduces the general power of Eq. (1.19) and (1.20) into

$$S_{\text{TM}} = \frac{1}{12\pi} (I_e dl)^2 \frac{\eta_0 \omega}{c} e^{-2\alpha r} \beta \times$$
$$\left[1 + \frac{\sqrt{2}}{|k|r} + \frac{2}{|k|^2 r^2} + \frac{\sqrt{2}}{|k|^3 r^3} \right] \tag{1.27}$$

$$S_{\text{TE}} = \frac{1}{12\pi} (I_m dl |k|)^2 \frac{c}{\eta_0 \omega} e^{-2\alpha r} \beta \left[1 + \frac{\sqrt{2}}{|k|r} \right] \tag{1.28}$$

In the near zone, the last terms in (1.19) and (1.27) are dominating, implying the Ohmic loss is proportional to the $|ka|^{-3}$ for electric dipole. Likewise, the last terms in (1.20) and (1.28) are dominating, implying the Ohmic loss is proportional to the $|ka|^{-1}$ for magnetic dipole antenna.

To provide a first hand intuition, calculated the numerical values of high-order terms in Eqs. (1.19) and (1.20), at 0.3m (near zone) and at 100m (far zone), respectively.

Table 2. Numerical values at $r = 100$m, far-zone

$\frac{2\alpha}{|k|^2 r}$	$\frac{1}{|k|^2 r^2}$	$\frac{\beta^2 - 3\alpha^2}{|k|^4 r^2}$	$\frac{2\alpha}{|k|^4 r^3}$
0.0796	0.0032	-0.0032	0.0252

In reference to the radiation term of unity, Table 1 and 2 listed numerical values of the high-order terms at 0.3m (near zone) and at 100m (far zone), respectively.

1.5.1 Exact analytic Ohmic loss in closed form and spherical lossy shell

It is well-known that in an open lossless medium, the Sommerfeld radiation boundary condition must be enforced [33], namely

$$lim_{r\to\infty}(\frac{\partial u(r,\theta,\phi)}{\partial r} - \mathrm{j}ku(r,\theta,\phi)) = 0 \qquad (1.29)$$

where $u(r,\theta,\phi)$ can be any component of E- or H-field. Physically, Eq. (1.29) forces the far zone field to decay in the rate of $\frac{1}{4\pi r}$, which is due to energy splitting along spherical surfaces.

In a homogeneous lossy medium, however, there is an additional decay factor of $e^{-2\alpha r}$ in (1.19) and (1.20) (and (1.27) and (1.28)), representing power loss owing to thermal dissipation. Comparing to lossless, decay in lossy environment will be more severely and rapidly. To quantitatively describe radiation efficiency of a dipole in a homogenous lossy medium, spherical lossy shell (SLS) is introduced. In [17] an SLS was defined, whose interior radius $r = a$ is source border and exterior radius $r = b$ was evaluated approximately such that 90% power has been dissipated. Nevertheless, this definition introduced a 10% uncertainty into a deterministic antenna problem. For the entire Ohmic loss to be considered by modifing the percentage into 100%, a closed form expression is derived in the following.

16

First the total power loss in the SLS from $r = a$ to $r = b$ is defined as

$$P_{\text{loss}}(b) := \frac{\sigma}{2} \int_a^b |\vec{E}_{\text{tot}}|^2 dv \qquad (1.30)$$

Employing Poynting theorem, the divergence of Poynting vector can be re-written

$$\vec{\nabla} \cdot (\vec{E} \times \vec{H}) = (\vec{\nabla} \times \vec{E}) \cdot \vec{H} - (\vec{\nabla} \times \vec{H}) \cdot \vec{E} \qquad (1.31)$$

From Ampere's law and Faraday's law, the second and third bracket are

$$\vec{\nabla} \times \vec{E} = -\frac{\partial \vec{B}}{\partial t} = -j\omega\mu_0\vec{H} \qquad (1.32)$$

$$\vec{\nabla} \times \vec{H} = \vec{J} + \frac{\partial \vec{D}}{\partial t} = (\sigma + j\omega\varepsilon')\vec{E} \qquad (1.33)$$

Then

$$\vec{\nabla} \cdot (\vec{E} \times \vec{H}^*) = -j\omega\mu_0|\vec{H}|^2 + j\omega\varepsilon'|\vec{E}|^2 - \sigma|\vec{E}|^2 \qquad (1.34)$$

Integrate both sides and make use of divergence theorem

$$\oint (\vec{E} \times \vec{H}) \cdot \vec{ds} = -\sigma \int |\vec{E}|^2 dv$$
$$-j\omega \int \mu_0|\vec{H}|^2 - \varepsilon'|\vec{E}|^2 dv \qquad (1.35)$$

Since the time-average power Poynting vector is half of its real part, the second volume integral above is pure imaginary and will disappear

$$S_{\text{avg}} = \frac{1}{2}\text{Re} \oint (\vec{E} \times \vec{H}^*) \cdot \vec{ds} = -\frac{\sigma}{2} \int |\vec{E}|^2 dv \qquad (1.36)$$

The above equation states that the total electromagnetic power though a close surface equal to the total Ohmic power loss. If ∂V_0 and ∂V_1 are spheres surface centered at the origin with arbitrary radius r_0 and r_1, respectively, and $r_0 < r_1$, the

total energy flow in closed region bounded by ∂V_0 and ∂V_1 is

$$\frac{1}{2}\text{Re}\oint_{r=r_0}^{r_1}\vec{E}\times\vec{H}^*\cdot\vec{ds} = \frac{1}{2}\text{Re}\left\{\oint_{r=r_1}\vec{E}\times\vec{H}^*\cdot\hat{r}ds\right.$$

$$\left.-\oint_{r=r_0}\vec{E}\times\vec{H}^*\cdot\hat{r}ds\right\}$$

$$=-\frac{\sigma}{2}\int_{r_0}^{r_1}|\vec{E}|^2dv \tag{1.37}$$

$$\Rightarrow P_{\text{tot}}(r_1)-P_{\text{tot}}(r_0) = -\frac{\sigma}{2}\int_{r_0}^{r_1}|\vec{E}|^2dv \tag{1.38}$$

Therefore the SLS Ohmic loss is equal to the difference of power flow at its interior and exterior borders, namely,

$$P_{\text{loss}}(b) := \frac{\sigma}{2}\int_a^b|\vec{E}_{\text{tot}}|^2dv = S|_{r=a}-S|_{r=b}. \tag{1.39}$$

where $S(r)$ for TM and TE were given in (1.19) and (1.20); no more integrations are needed when evaluating the power loss in an SLS, which removed math difficulty and preserved pin-point accuracy up to 4th decimal point. Consequently, the entire Ohmic loss is considered by modified the percentage into 100%.

Numerical data strongly support our derivations and is quoted below. Using numerical and integration by parts, the total Ohmic losses are

$$P_{\text{TM},100\%} = \frac{\sigma}{2}\int_a^\infty\left|\vec{E}_{\text{tot}}\right|^2dv = 0.2458(I_edl)^2 \tag{1.40}$$

$$P_{\text{TE},100\%} = \frac{\sigma}{2}\int_a^\infty\left|\vec{E}_{\text{tot}}\right|^2dv = 0.3401(I_mdl)^2 \tag{1.41}$$

Comparing to Poynting power (1.19) and (1.20) to the Ohmic losses (1.40) and (1.41)

$$S_{\text{TM}}(r=a) = 0.2458(I_edl)^2 \tag{1.42}$$

$$S_{\text{TE}}(r=a) = 0.3401(I_mdl)^2 \tag{1.43}$$

one can see

$$P_{\text{TM},100\%} = S_{\text{TM}}(a) \tag{1.44}$$

$$P_{\text{TE},100\%} = S_{\text{TE}}(a) \tag{1.45}$$

1.5.2 Antenna radiation efficiency

Radiation efficiency of an antenna is defined as the ratio of radiated power to total source power (sum of radiated and ohmic power), namely

$$\eta_r(b) = \frac{P_{\text{rad}}(b)}{P_{\text{rad}}(b) + P_{\text{loss}}(b)} = \frac{1}{1 + \frac{P_{\text{loss}}(b)}{P_{\text{rad}}(b)}} \tag{1.46}$$

where $P_{\text{loss}}(b)$ is power loss in the SLS of $r = b$ defined in (1.39), and $P_{\text{rad}}(b)$ is radiated power passing sphere of $r = b$ which is the 1st term of (1.19) or (1.20), (or (1.27) and (1.28)). Notice that $\eta_r(b)$ depends on the field point, i.e., radius of the exterior border of the SLS. As radiation is concerned, b is in the far-zone. From Figs. 2 (a) and 2 (b), $b \geq \lambda$.

Before evaluating $\eta_r(b)$, let us consider the power ratio in (1.46). For a highly lossy medium, the TM case,

$$
\begin{aligned}
\frac{P_{\text{loss}}^{\text{TM}}(b)}{P_{\text{rad}}(b)} =& \frac{S_{\text{TM}}(a) - S_{\text{TM}}(b)}{S_{\text{TM}}(b)} \\
=& e^{2\alpha(b-a)} \left(1 + \frac{\sqrt{2}}{|k|a} + \frac{2}{|k|^2 a^2} + \frac{\sqrt{2}}{|k|^3 a^3} \right) - \\
& \left(1 + \frac{\sqrt{2}}{|k|b} + \frac{2}{|k|^2 b^2} + \frac{\sqrt{2}}{|k|^3 b^3} \right)
\end{aligned}
\tag{1.47}
$$

Similarly, for TE case

$$\frac{P_{\text{loss}}^{\text{TE}}(b)}{P_{\text{rad}}(b)} = \frac{S_{\text{TE}}(a) - S_{\text{TE}}(b)}{S_{\text{TE}}(b)}$$

$$= e^{2\alpha(b-a)}\left(1 + \frac{\sqrt{2}}{|k|a}\right) - \left(1 + \frac{\sqrt{2}}{|k|b}\right) \tag{1.48}$$

Let $a = 0.3$m and $b = 100$m, the ratios above can be approximated by its dominant term, yielding

$$\frac{P_{\text{loss}}^{\text{TM}}(b)}{P_{\text{rad}}(b)} \approx e^{2\alpha(b-a)}\frac{\sqrt{2}}{|k|^3 a^3} \gg 1$$

$$\frac{P_{\text{loss}}^{\text{TE}}(b)}{P_{\text{rad}}(b)} \approx e^{2\alpha(b-a)}\frac{\sqrt{2}}{|k|a} \gg 1$$

Finally estimate (1.46) as

$$\eta_r^{\text{TM}}(b) = \frac{1}{1 + e^{2\alpha(b-a)}\frac{\sqrt{2}}{(|k|a)^3}} \approx e^{-2\alpha(b-a)}\frac{(|k|a)^3}{\sqrt{2}} \tag{1.49}$$

$$\eta_r^{\text{TE}}(b) = \frac{1}{1 + e^{2\alpha(b-a)}\frac{\sqrt{2}}{|k|a}} \approx e^{-2\alpha(b-a)}\frac{|k|a}{\sqrt{2}} \tag{1.50}$$

From discussions above, it is obvious that the radiation efficiency of TM mode is proportional to $(|k|a)^3$ and TE mode is proportional to $|k|a$. It is seen that the efficiency of TM is 1.42106×10^{-15} and TE is 5.00451×10^{-13}. In term of antenna efficiency, the TE case is about 352 times better than TM case.

1.5.3 Source requirement

The DARPA AMEBA requires to deliver 100fT magnetic flux density undersea to 100m (far-zone) at 1 kHz. It demands the source to be
TM:

$$\mu_0|\vec{H}| = \mu_0\frac{I_e dl}{4\pi r}|k|e^{-\alpha r} = 10^{-13}$$

$$\Rightarrow I_e dl = (10^{-13})\frac{4\pi r}{\mu_0|k|}e^{+\alpha r} = 160.4$$

Table 3. Required source power for under seawater dipoles

TM	TE
$I_e dl = 160.4 \text{Am}$	$I_m dl = 7.12687 \text{Vm}$
$P_{\text{TM}} = 6.324 \times 10^3 \text{W}$	$P_{\text{TE}} = 17.2745 \text{W}$

Using (1.40), the required source power

$$P_{\text{TM}} = 0.2458 (I_e dl)^2 = 0.2458 \times 160.4^2 = 6323.98 \text{W}$$

TE:

$$\mu_0 |\vec{H}| = \mu_0 \frac{I_m dl}{4\pi r |\eta|} |k| e^{-\alpha r} = 10^{-13}$$

$$\Rightarrow I_m dl = (10^{-13}) \frac{4\pi r \eta_0}{\mu_0 k_0 |\varepsilon_r|} e^{\alpha r} = 7.12687$$

Using (1.41), the required source power

$$P_{\text{TE}} = 0.3401 (I_m dl)^2 = 0.3401 \times 7.12687^2 = 17.2745 \text{W}$$

The numerical values for dipole moment ($I_e dl$ or $I_m dl$) and required power of the source are tabulated in Table 3. It shows that the required power of magnetic dipole is less than that of electric dipole in two to three orders of magnitude.

Since the required current moment, $I_m dl$, is 7.12687Vm and a linear dipole has an effective length of half its physical length, the magnetic current, I_m, required to deliver the 100fT to 100m under sea is 23.7562V. Under assumption that magnetic field is uniform within the permeable dipole core, and with current loop feeding, the magnetic current moment of an N-turn loop is

$$I_m dl = N\omega \mu_0 \mu_r I_{loop} A \qquad (1.51)$$

where I_{loop} is the electric loop current around the magnetic core and A is the cross-section area of the core.
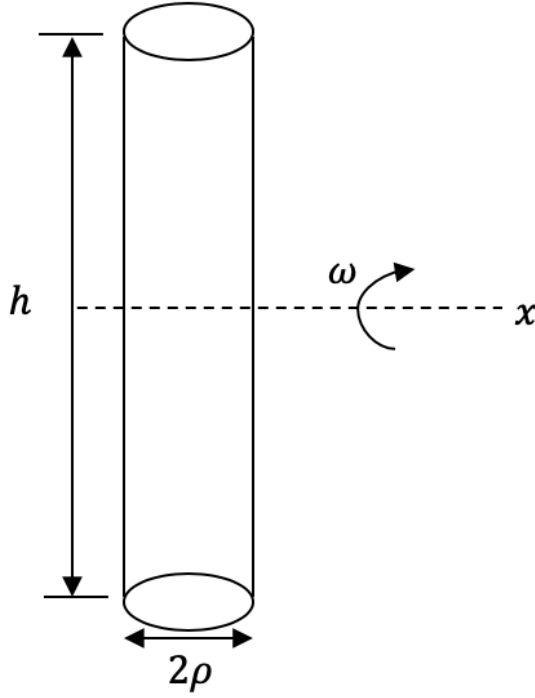
Figure 6. Moment of inertia for cylinder rotating along x-axis

1.6   Mechanically Spinning Dipole

This section studies a mechanically spinning dipole from viewpoint of tuning and impedance matching. A mechanically rotating dipole at 1000 cycle per second may radiate EM waves at 1 kHz; no particular resonant circuit need be built to attain the frequency. Although ordinarily it is assumed that antennas with physical size much smaller than the wavelength are difficult to tune and match. Alternatively, permeable antenna of the kind has been recently demonstrated to exhibit good efficiency in low impedance environments [28].

Figure 6 depicts a dipole spinning at angular frequency ω along x-axis, with its ends tracing a circle of radius $h/2$. It can be determined from [34] that the current

moment produced by the spinning dipole is

$$I_{e,m}dl = Q_{e,m}\omega h \tag{1.52}$$

The effective charge at the ends of a permanently polarized material (magnet or electret) is

$$Q_{e,m} = P_{e,m}A \tag{1.53}$$

where $P_{e,m}$ is the polarization density, and A is the cross section. To radiate at 1kHz, the dipole may spin at 60,000 rpm. The kinetic energy for such rotational dipole is

$$K_e = \frac{1}{2}J_k\omega^2 \tag{1.54}$$

where the moment of inertia is $J_k = \frac{1}{12}M(h^2 + 3\rho^2)$ for cylinder with height h, mass M and radius ρ shown in Fig. 6.

Since the kinetic energy limit is 5000 Joules from AMEBA requirement, the moment of inertia

$$J_k = \frac{5,000}{\frac{1}{2}\omega^2} = 2.533 \times 10^{-4} \text{kg} \cdot \text{m}^2$$

Choose $h = 2\rho$ for square longitudinal cross-section, yielding kinetic energy

$$\frac{1}{12}M(h^2 + \frac{3}{4}h^2) = 2.533 \times 10^{-4}$$

$$\Rightarrow \frac{7}{48}Mh^2 = 2.533 \times 10^{-4} \text{kg} \cdot \text{m}^2 \tag{1.55}$$

and the mass density

$$\frac{M}{0.25\pi h^3} = D \times 10^3 \text{kg} \cdot \text{m}^{-3} \tag{1.56}$$

where D is material density in g/cm^3. Dividing (1.55) by (1.56)

$$\frac{7\pi}{192}h^5 = \frac{2.533 \times 10^{-7}}{D}$$

$$\Rightarrow h = \left(\frac{4.8634 \times 10^{-5}}{7\pi D}\right)^{\frac{1}{5}} \tag{1.57}$$

For NdFeB magnets $D = 7.5$, ceramic electrets $D = 3.8$, and carbon fiber $D = 1.5$, the corresponding cylinder height $h_m = 0.0494$m, $h_e = 0.0566$m, and $h_c = 0.0682$m. This means the spinning dipole has required height h in the order of 0.05m and cross-section of $\pi\rho^2 = 1.9635 \times 10^{-3}$m^2, and volume of 9.8175×10^{-5}m^3 for stored kinetic energy of 5 Kilo Joules spinning at 60 000 rpm.

For electric dipole, using today's best electrets with $P_e = 0.034$C/m^2, the source

$$I_e dl = 2P_e A\omega\rho = 0.02097\text{A} \cdot \text{m}$$

and for magnetic dipole with today's best magnet of saturation magnetization $M_s = 1.15 \times 10^6$ A/m, the corresponding $P_m = \mu_0 M_s = 1.4451T$,

$$I_m dl = 2P_m A\omega\rho = 0.8914\text{V} \cdot \text{m}$$

Using (1.40) and (1.41), the total source power is 1.081×10^{-4}W for TM case and 0.2702W for TE case. The data suggest that spinning magnet operating at 1 kHz may produce $100 \times 0.8914/7.12687 = 12.51 f$T magnetic field at 100 m, and this antenna operates within 5 kJ of kinetic energy. Further calculations indicate that it requires mechanical power of 220 W to compensate ball bering friction loss [29].

1.7   Design of magnetic dipole antenna

From previous discussions, the electric dipoles encounter too much Ohmic power. Dipole of mechanically spinning electrets/magnets cannot provide required H-field level under pre-specified kinetic energy unless the dipole is replaced with quadrupoles. Therefore, the magnetic dipole is chosen. It is called permeable antenna, which is a ferrite cylinder with loop current as source.
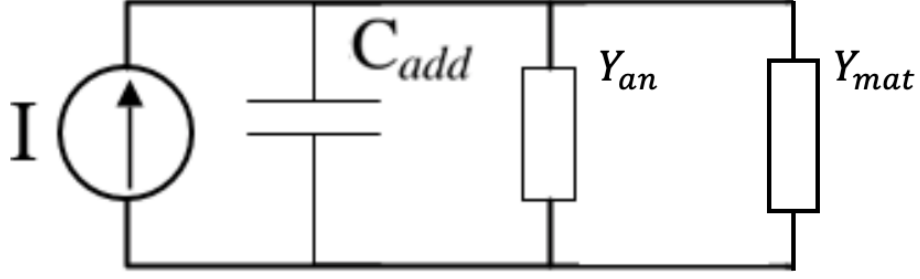
Figure 7. Input admittance equivalent circuit of permeable dipoles with added matching capacitor

The input admittance of a permeable dipole can be evaluated using lumped circuit model [28]. The equivalent circuit is shown in Fig. 7, where Y_{mat} represents input admittance caused by internal dipole material, Y_{an} is for wire antenna input admittance, and Y_{cap} for external tuning capacitor. Assuming the current distribution on a electrically small dipole is linear, the input admittance simply becomes

$$
\begin{aligned}
Y_{\text{in}} =& Y_{\text{mat}} + Y_{\text{an}} + Y_{\text{cap}} \\
=& Y_{\text{mat}} + \frac{\mathrm{j}\omega\varepsilon_0 l}{6\pi} \ln\left(\frac{l}{2\rho}\right) + \frac{1}{\frac{\mathrm{j}\omega\pi\mu_0 l}{2\ln\left(\frac{l}{2\rho}\right)}} + \frac{20(kl)^2}{\eta^2}
\end{aligned}
\tag{1.58}
$$

where

$$
Y_{\text{mat}} = \frac{1}{\mathrm{j}\omega\mu_0(\mu_r - 1)\frac{\pi\rho^2}{l}} + \frac{\mathrm{j}\omega\varepsilon_0(\varepsilon_r - 1)l}{8\pi}, \rho = 0.1\text{m}, l = 0.6\text{m}
$$

For non-linear current distribution, the input admittance of the dipole can be modeled as RLC circuit [35], the parameter for each components are

$$
\begin{aligned}
R_{\text{an}} &= 80\pi^2 \left(\frac{2l_{\text{eff}}}{\lambda}\right)^2 \\
L_{\text{an}} &= \frac{1}{|I_{\text{in}}|^2} \int_0^l \frac{\mu}{\pi} \log \frac{2z}{\rho} |I(z)|^2 dz \\
C_{\text{an}} &= \frac{\pi\epsilon l}{2\log\left(\frac{l}{2\rho}\right)}
\end{aligned}
\tag{1.59}
$$

where the effective length is

$$l_{\text{eff}} = \frac{1}{I_{\text{in}}} \int_0^l I(z)dz$$

1.8 Summary

This section investigated multi-physics generated small dipoles in homogeneous lossy medium in the ULF-VLF bands. The study shows that the radiation efficiency, η_r, is proportional to $|ka|^3$ for TM and $|ka|$ for TE dipole, respectively. Therefore, the required source power for TE is two to three orders of magnitude less than that of TM. Numerical results indicate that to deliver 1 kHz radio signal undersea at distance of 100 m (far-zone) with a minimum 100 fT magnetic flux density, the TM dipole requires 6.324 kW of source power. In contrast, the TE dipole demands only 17.27 W of source power, which means the radiation efficiency of TE is 350 times better than TM case.

Dipoles of mechanically spinning electrets/magnets are smaller than their counter-partners of TE/TM antennas in physical size and weight, but may produce less than required field intensity in the far-zone. Antennas based on spinning electrets or magnets may need their rotation speed to be 60,000 cycles per minute. To implement any mechanically driving antennas, the precision flying wheel is a must.

More attention was given to the TE dipole, referred to as the permeable antenna, including feeding, tuning and matching circuits. Next chapter will focus on solving the unknown current distribution on the wire antenna using MoM. After that, the input impedance and matching network can be calculated easily.

Chapter 2

RIGOROUS ANALYSIS OF WIRE ANTENNAS BY COMBINED EFIE AND
WAVELETS

2.1   Introduction

Current distribution on a wire antenna is the key to find basic antenna parameters
such as input impedance, near and far electromagnetic fields, antenna gain, radiation
pattern, etc. The current on a thin dipole is assumed to be sinusoidal [36]. It seems
a good approximation for simple structure, but shows lack of theoretical basis on
general antennas. For this reason, numerical methods such as Moment of Methods
(MoM) are used to solve the current distribution in arbitrary antenna structure with
good accuracy [37].

For wire antennas, many papers have been published [38], [39] but the problems
are limited to 1D complexity and use different source and observe axis to avoid the
singularity problem. For a fat wire antenna with finite and non-negligible radius, a
more accurate model has appeared [7]. To replace the traditional delta-gap source, a
more accurate source model is developed by using the Huygens' principle. From this
principle and reciprocity theorem, a variational formulation of the input admittance is
derived. When the triangle function is chosen as both basis and weighting functions,
all the elements of impedance matrix and source vector are formulated in closed forms.
Both Electric- and magnetic- current Green's functions are used to form an EFIE.

At first the Electric Field Integral Equation (EFIE) equation is derived with
unknown surface current vectors. Then using Galerkin's method with triangle and

27

Coifman wavelets (Coiflets) to construct the impedance matrix and source vector. Finally, solving the unknown current from MoM. Other antenna parameters can be easily computed. In this chapter we will extend this model and combine with intervallic wavelets.

2.2 Formulation

To solve for the unknown current distribution of the dipole [7], the integral equation to be solved is

$$j\omega\mu \oint_S dS' \bar{\boldsymbol{G}}_e(\vec{r},\vec{r}') \cdot \vec{J}(\vec{r}') = -\nabla \times \oint_{S_a} dS' \vec{\boldsymbol{G}}_m(\vec{r},\vec{r}') \cdot \vec{M}_a(\vec{r}') \tag{2.1}$$

where $\bar{\boldsymbol{G}}_e(\vec{r},\vec{r}')$ and $\bar{\boldsymbol{G}}_m(\vec{r},\vec{r}')$ are electric- and magnetic- field dyadic Green's functions, $\vec{M}_a$ is magnetic current equivalent of source feeding at the gap, $\vec{J}(\vec{r})$ is the induced current of the dipole to be solved. Next decomposing the current into linear combination of basis functions with unknown coefficients

$$\vec{J}(\vec{r}) = \sum_{n=1}^{n} I_n \vec{J}_n(\vec{r}) \tag{2.2}$$

If Galerkin's method is used, the impedance matrix becomes

$$Z_{mn} = j\omega\mu \langle \vec{J}_m(\vec{r}), \bar{\boldsymbol{G}}_e(\vec{r},\vec{r}'), \vec{J}_n(\vec{r}') \rangle \tag{2.3}$$

And the source vector beomes

$$V_m = -\langle \vec{J}_m(\vec{r}), \nabla \times \bar{\boldsymbol{G}}_m(\vec{r},\vec{r}'), \vec{M}_a(\vec{r}') \rangle \tag{2.4}$$

Under the assumption that the gap and radius of the dipole antenna are electrically small, the dyadic Green's function can be simplified, resulting the impedance matrix

28

to be well-known Pocklington's integral equation in 2D

$$Z_{mn} = -\frac{jk\eta}{16\pi^3}\int_{\Delta S_m}\int_{\Delta S_n}\vec{J}_m(z)\cdot\vec{J}_n(z')g(\vec{r}-\vec{r'})dS'dS$$

$$+\frac{j\eta}{16\pi^3 k}\int_{\Delta S_m}\int_{\Delta S_n}\frac{d}{dz}J_m(z)\frac{d}{dz'}J_n(z')g(\vec{r}-\vec{r'})dS'dS \qquad (2.5)$$

where the Green's function

$$g(\vec{r}-\vec{r'}) = \frac{e^{-jkR}}{R}$$

$$R = |\vec{r}-\vec{r'}| = \sqrt{2\rho^2(1-\cos(\phi-\phi'))+(z-z')^2}$$

It is worth-noting that the second part of (2.5) involves of differentiation on the basis functions. The derivatives of triangle basis functions are simple and well defined. But they may be problematic for other basis such as Daubechies wavelets where the derivatives do not exist. One way to avoid solving the derivatives inside the Z matrix integration is by using integral by parts to move the differentiation operator onto the Green's functions instead of the basis functions. Since the basis functions have no azimuth angle, ϕ, dependence, it can be moved out of the integral and is only integrated along z direction. Assume that the basis functions are along z direction and zero at both ends

$$\int_{\Delta z}\int_{\Delta z'}\frac{d}{dz}J_m(z)\frac{d}{dz'}J_n(z')g(\vec{r}-\vec{r'})dz'dz = \int_{\Delta z}\int_{\Delta z'}J_m(z)J_n(z')\frac{\partial^2}{\partial z\partial z'}g(\vec{r}-\vec{r'})dz'dz$$

$$(2.6)$$

Evaluate the derivatives

$$\frac{\partial}{\partial z}R = -\frac{\partial}{\partial z'}R = \frac{z-z'}{R}$$

$$\frac{\partial}{\partial z'}g = \frac{e^{-jkR}(1+jkR)(z-z')}{R^3}$$

$$\frac{\partial^2}{\partial z\partial z'}g = \frac{[k^2 e^{-jkR}(z-z')^2+e^{-jkR}(1+jkR)]R^2-3[e^{-jkR}(1+jkR)(z-z')](z-z')}{R^5}$$

The result integral has no basis functions' derivatives is

$$\int_{\Delta z}\int_{\Delta z'}\frac{d}{dz}J_m(z)\frac{d}{dz'}J_n(z')g(\vec{r}-\vec{r'})dz'dz$$

$$=\int_{\Delta z}\int_{\Delta z'}J_m(z)J_n(z')\times$$

$$\frac{[k^2e^{-jkR}(z-z')^2+e^{-jkR}(1+jkR)]R^2-3[e^{-jkR}(1+jkR)(z-z')](z-z')}{R^5}dz'dz$$

$$(2.7)$$

Now any basis function can be used to evaluate the Z matrix. However, the trade-off is that (2.7) becomes much more singular than the integral in (2.5), $\mathcal{O}(R^{-1})$vs.$\mathcal{O}(R^{-3})$.

2.3   Basis functions

Before solving the MoM system, the basis functions have to be chosen. This section will include both triangle basis functions and Coifman wavelets (Coiflets). The triangle basis functions are used in [7] and shows good agreements with measurements. But as basis function, triangle is not orthogonal and needed to be normalized, which is superior to Coiflets which is complete orthonormal basis and have vanishing moments up to L order.

2.3.1   Triangle basis functions

The triangle basis function is shown in Fig. 8.The advantages of triangle basis functions are easy to calculate and shown good results. But triangle functions are not well-defined basis because they are not orthogonal to each other. The sharp edge of the triangles can also introduce fictitious charges. The triangle basis function is
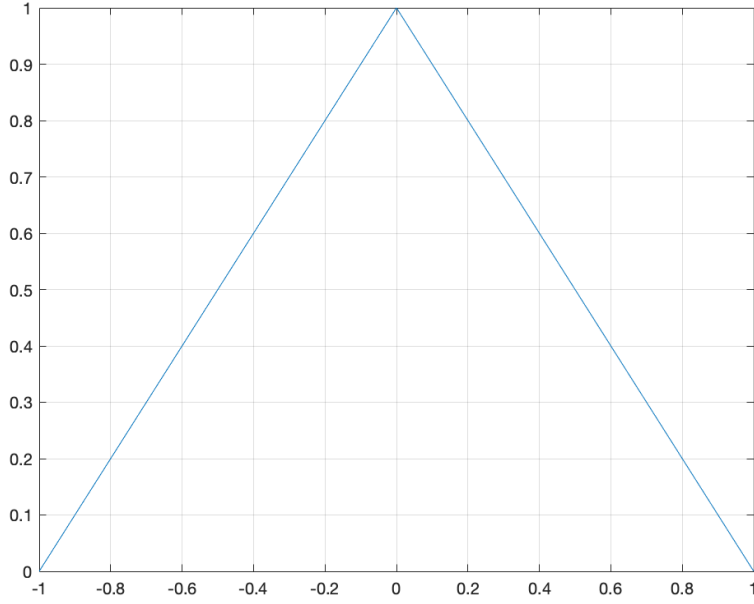
Figure 8. Triangle basis function

defined as

$$\phi(x) = 1 - |x|, \ \ x \in [-1, 1] \tag{2.8}$$

2.3.2 Coifman wavelets

The other basis function is Coiflets of order $L = 4$ shown in Fig. 9. The Coiflets are orthonormal basis functions with $L - 1$ and L vanishing polynomial moments, meaning $\int_{-\infty}^{\infty} x^l \phi(x) = 0, l = 0, 1, ..., L - 1$. There is no sharp edge that can introduce fictitious charge.
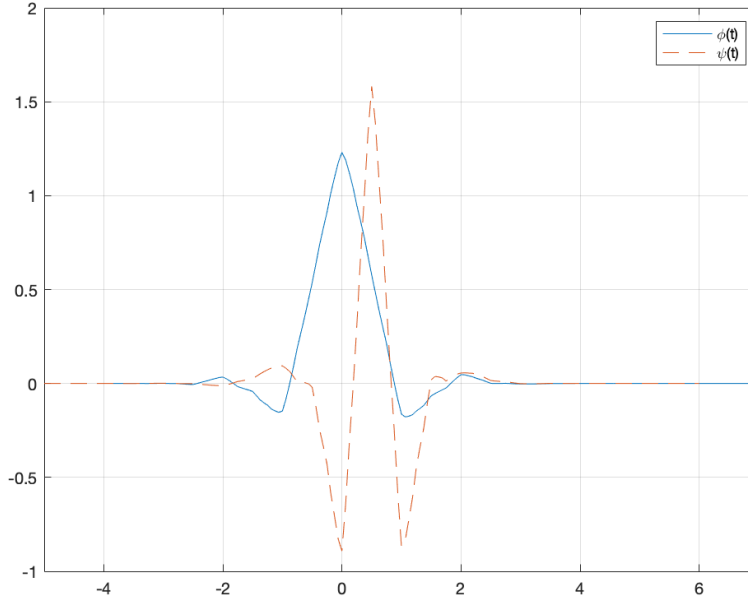
Figure 9. Coiflets scalet ϕ and wavelet ψ $(L = 4)$

2.4 Current distribution from MoM

Before constructing the MoM matrix, the basis function resolution is chosen to span the entire antenna region. The basis function with order j resolution is given by

$$\phi_{j,k}(x) = 2^{j/2}\phi(2^j x - k) \tag{2.9}$$

2.4.1 Dipole antenna

To solve the MoM system for the short dipole, let the dipole to be 0.5m long, radius $\rho = 0.02$m, and the gap due to feeding is $\Delta = 0.0227$m. For a half-wavelength dipole, evaluating current distribution at $f = 300MHz$ using triangle and Coiflets basis functions of oder $j = 5$, then compare with 1D MoM from [38]. The results

32
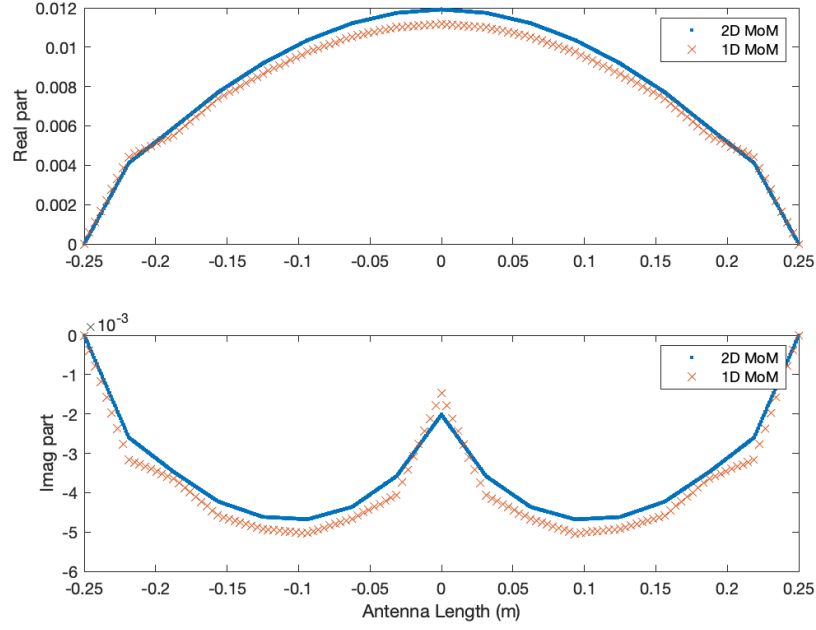
Figure 10. Current distribution on dipole antenna at 300MHz using triangle basis

are shown in Fig. 10 and Fig. 11, respectively, where 2D MoM refers to the fully integrations in 2.5 and 1D MoM refers to only integrate on the source [38].

For an electrically small dipole, the current distribution at $f = 1kHz$ using triangle and Coiflets basis functions of oder $j = 5$ are shown in Fig. 12 and Fig. 13, respectively. The current on an electrically short dipole is usually assumed linear, which mostly agree with results from MoM. However, as the radius increase, such linearly approximation may not be true and MoM should be used for better results.
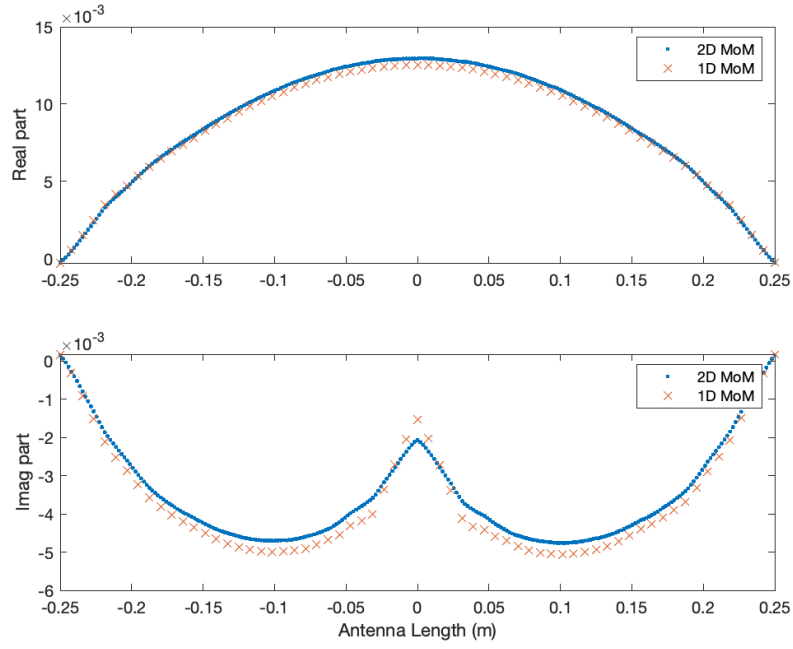
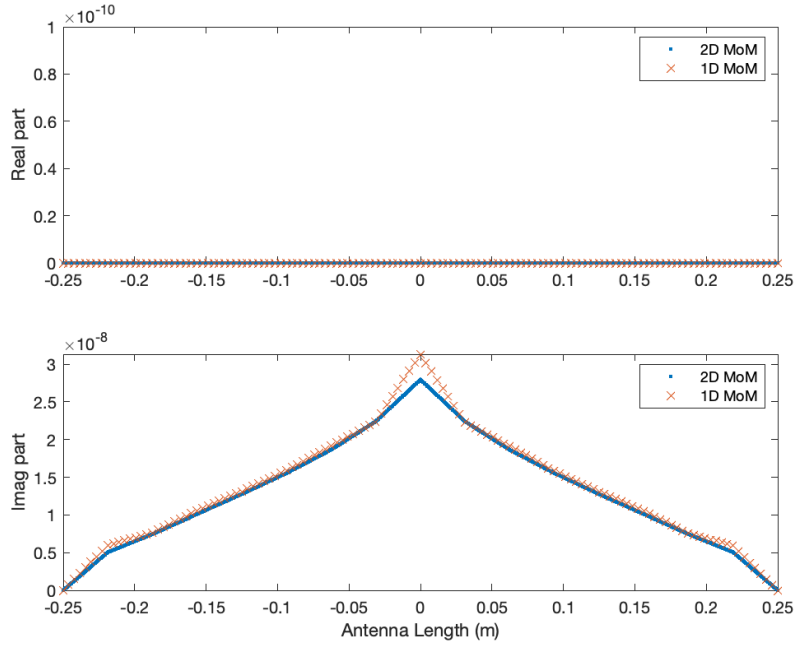Figure 11. Current distribution on dipole antenna at 300MHz using Coiflet basis

Figure 12. Current distribution on loop antenna at 1kHz using triangle basis

Figure 13. Current distribution on loop antenna at 1kHz using Coiflet basis

2.4.2   Loop antenna

The current distribution for a loop antenna can be found using similar method. To evaluate the inner product of basis functions and their distances, let first clarify the coordinate system, shown in Fig. 14, where A is the loop radius and

$$\vec{R} = (A\cos\phi + a\cos\alpha\cos\phi)\hat{x} + (A\sin\phi + a\cos\alpha\sin\phi)\hat{y} + (a\sin\alpha)\hat{z}$$

$$\vec{R}' = (A\cos\phi' + a\cos\alpha'\cos\phi')\hat{x} + (A\sin\phi' + a\cos\alpha'\sin\phi')\hat{y} + (a\sin\alpha')\hat{z}$$

$$\vec{J}(\vec{R}) = J(\vec{R})(-\sin\phi\hat{x} + \cos\phi\hat{y})$$

$$\vec{J}(\vec{R}') = J(\vec{R}')(-\sin\phi'\hat{x} + \cos\phi'\hat{y}) \tag{2.10}$$

Substitute (2.10) into the same integral equation, solving the current on loop. Let the loop perimeter to be 0.5m long, radius $\rho = a = 0.02$m, and the feeding
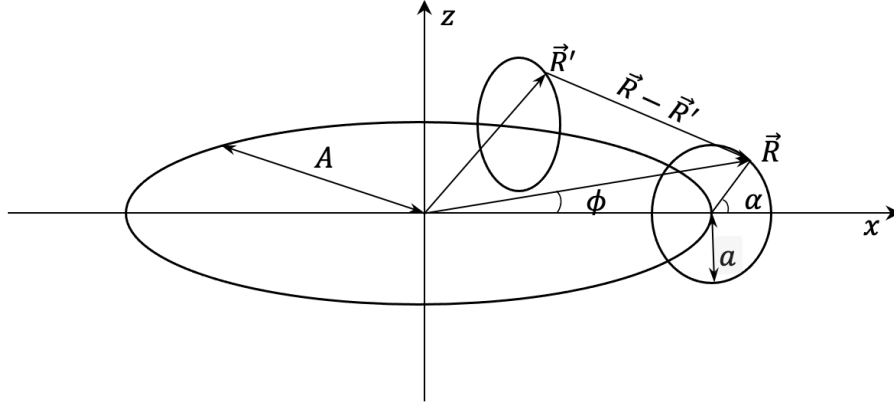
Figure 14. Loop antenna coordinate system

gap is $\Delta = 0.0227$m. At frequency $f = 300$MHz, the current distributions using triangle and Coiflets basis functions are shown in Fig. 15 and Fig. 16, respectively. The current distributions agree well with results in [38]. Since the perimeter is half of the wavelength, the antenna input impedance approaches to infinity due to antiresonance [40].

Again, for electrically small antenna, the current distribution on loop antenna is expected to behave like DC. After solving the MoM system, The current distribution at $f = 1kHz$ using triangle and Coiflets basis functions are shown in Fig. 17 and Fig. 18, respectively. The currents are almost constant on entire loop as expected. The calculated input impedance is $0.00 + 0.0010j$ for both basis functions. From [41], the inductance of a small loop antenna is

$$L = \mu\sqrt{A(A-a)}\left[\left(\frac{2}{k} - k\right)K(k) - \frac{2}{k}E(k)\right] \tag{2.11}$$

where

$$k^2 = \frac{4A(A-a)}{(2A-a)^2} \tag{2.12}$$

K and E are the elliptic integrals of the first and second kinds.

36

Figure 15. Current distribution on loop antenna at 300MHz using triangle basis

Figure 16. Current distribution on loop antenna at 300MHz using Coiflet basis

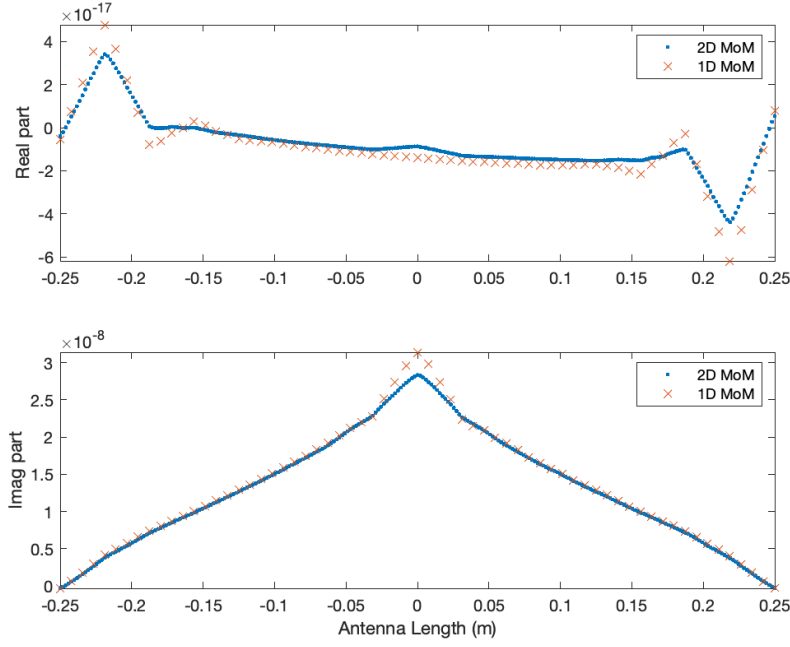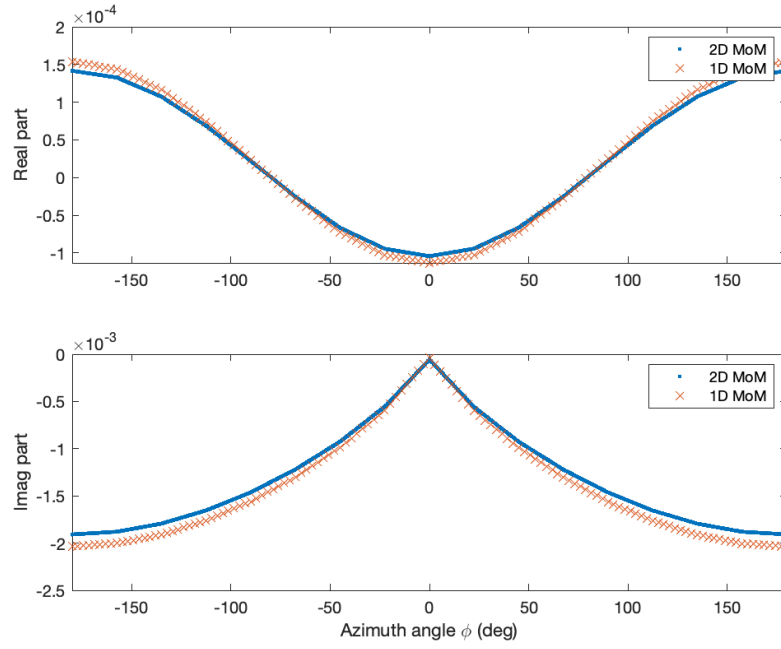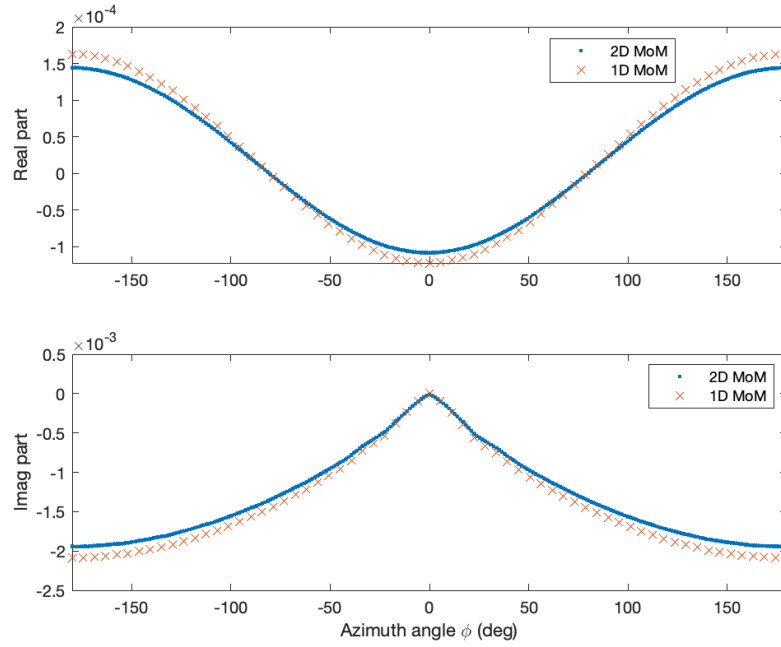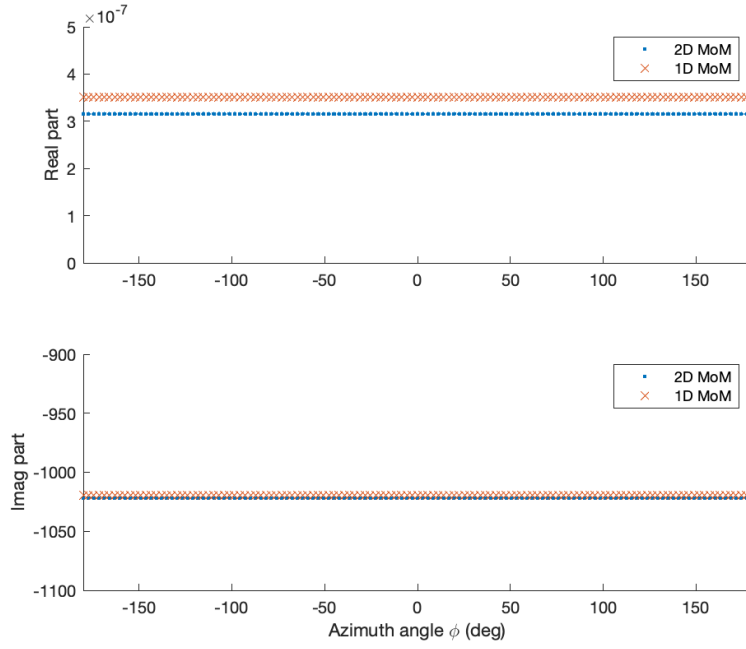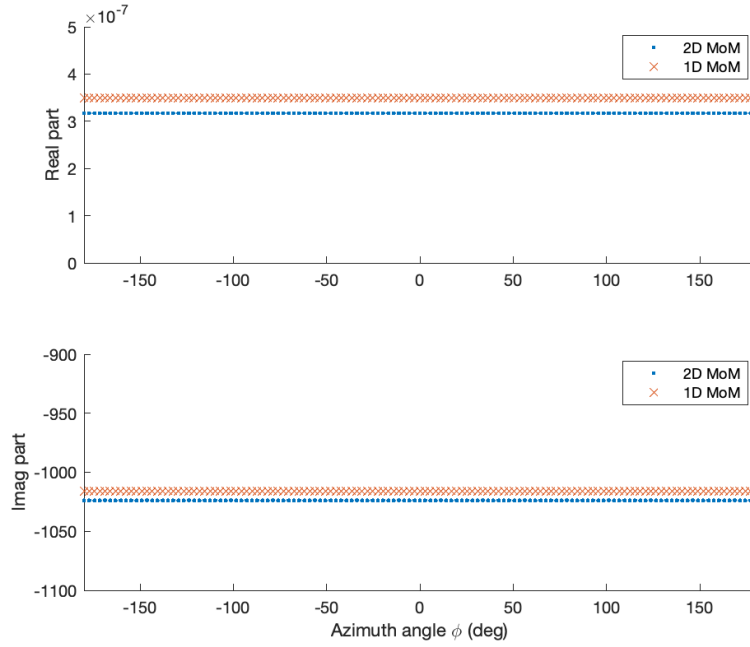Figure 17. Current distribution on loop antenna at 1kHz using triangle basis

Figure 18. Current distribution on loop antenna at 1kHz using Coiflet basis

2.5　Input impedance

After the current distribution is calculated from MoM in the previous section, the input impedance due to antenna itself can be found by

$$Z_{MoM} = \left(\frac{1}{V_a^2} \sum_n I_n V_n \right)^{-1} \tag{2.13}$$

where V_a is the applied source voltage at the gap. The MoM results are compared with [35] where sinusoidal current distribution is assumed and shown below

$$R_{an} = 80\pi^2 \left(\frac{2l_{eff}}{\lambda} \right)^2$$

$$C_{an} = \frac{\pi \varepsilon L}{2 \ln(L/a)}$$

$$L_{an} = \frac{1}{|I_0|^2} \int_0^{L/2} \frac{\mu}{\pi} \ln \left(\frac{2z}{a} \right) |J(z)|^2 dz$$

$$Z_{book} = R_{an} + \frac{1}{j\omega C_{an}} + j\omega L_{an} \tag{2.14}$$

The result is shown in Table 4 where Z_{tri} and Z_{coif} are input impedance calculated by MoM with triangle and Coiflets basis functions, respectively, Z_{book} is input impedance calculated from (2.14).

The results from MoM are close to each other and should approach to book values when the wire radius reduces. At $a = 1$mm and feeding gap $\Delta = 5$mm, the input impedance using MoM becomes 71.6 +23.4j, which is comparable to the value of 73.14Ω for infinitesimal thin antenna [42]. When the length is near 0.48λ, the imaginary part of input impedance should approach to zero. The MoM impedance value is $72.4 - 1.21j$ is obtained for a dipole antenna with $L = 0.48\lambda$ and $L/(2a) = 100$, similar to Collin's measurement and theoretical values.

Assume the antenna length, $L = 0.5$m, wire radius, $a = 2$mm. For the NiZn ferrite tile material with permittivity $\varepsilon_r = 14 - j0.14$ and permeability $\mu_r = 2000$,

Table 4. Numerical input impedance values

	$L = 0.5$m $f = 300$MHz $a = 15$mm	$L = 0.5$m $f = 300$MHz $a = 2$mm	$L = 0.5$m $f = 1$kHz $a = 15$mm	$L = 0.5$m $f = 1$kHz $a = 2$mm
Z_{tri}	91.6 +27.3j	81.7 +20.0j	1.73e-03 - 5.32e+07i	1.42e-03 - 9.79e+07i
Z_{coif}	87.6 +28.4j	83.1 +29.6j	1.06e-01 - 4.93e+07j	1.02e-01 - 9.70e+07j
Z_{book}	80.0 -86.0j	80.0 -50.2j	2.19e-09 - 8.03e+07j	2.19e-09 - 1.26e+08j
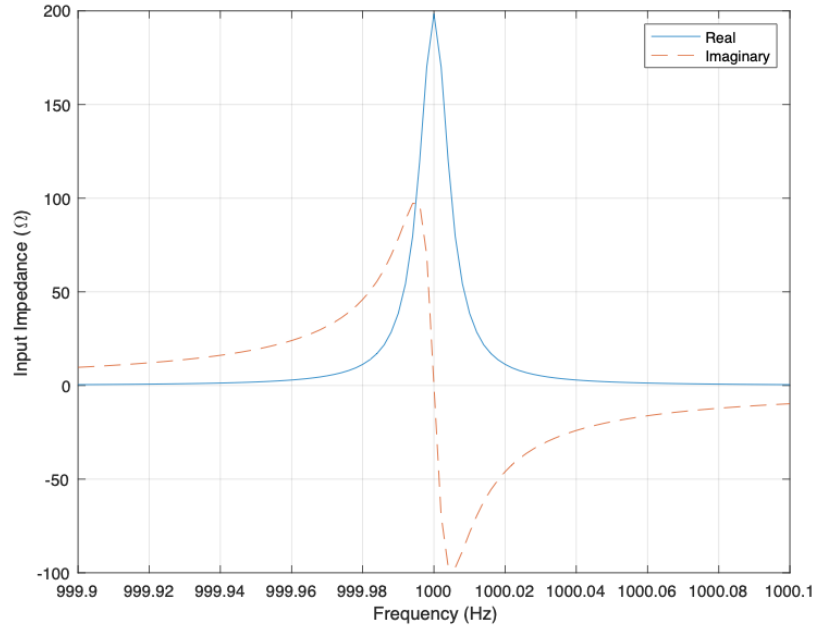
Figure 19. Input admittance of designed dipole with 159.3mF shunt capacitor matching

the resulting input impedance is shown in Fig. 19 with 159.3mF shunt capacitor, which is common value for aluminum electrolytic capacitors. The resulting antenna's resonance lies at 1kHz.

In order to feed the dipole, a solenoid is used. The required current is found from (1.51) at approximate. It requires turn-current product $NI = 14.3658$A $\cdot$ turn, which is moderate current and can be easily achieved from copper wires. For example, the

wire of American Wire Gauge (AWG) number 7 has wire diameter of 3.66522mm and can withstand maximum current of 30A with maximum frequency of 1300Hz. Increasing loop number can further reduce the current at the feeding.

2.6 Summary

In this chapter, the MoM with both triangle and Coifman wavelets are used to solve the antenna current distribution on dipole and loop antenna. They shows good agreement with each other and published papers. More attention was given to the TE dipole, referred to as the permeable antenna, including feeding, tuning and matching circuits. For high efficiency permeable TE antennas, the tuning/matching network requires high voltage capacitors in milli-faradays, which are 1000 times larger than commercially available products. The turn-current is $14.37\text{A}\cdot\text{turn}$ which is compatible with AWG7 wire.

Chapter 3

ON MODELING AND MEASUREMENT OF GCPW FOR AUTOMOTIVE
RADAR APPLICATIONS

3.1 Introduction

Millimeter wave radars have appeared in the scene as safety devices for cruise control, automatic braking and collision warning. The GCPW is used to deliver power from the source to antennas. Power loss at millimeter wave frequencies are significant, which attenuates the weak signals and degrades system performances. Many papers reported that transmission lines, including micro strip, strip line, coplanar waveguide (CPW), substrate integrated waveguide (SIW), among others, may produce severe loss of 103 dB/m in the V-band of 52-75 GHz frequency range [43]. In this chapter, model the GCPW using semi-analytical method, and simulate the structure with commercial EM software, HFSS of the ANSYS.

The laboratory measurements are conducted in 75 to 90 GHz, using Rohde & Schwarz ZVA24 VNA along with MOL V10VNA2 frequency extension modules. One-port and two-port calibrations are discussed in details. Mis-alignment becomes problem in high frequency measurement as wavelength shrinking to the millimeter range. As a result, the original system is embedded with error boxes which need to be de-embedded. Many matured techniques are available for such problem if the device under test (DUT) is one-port. But few papers devoted to two-port devices. In this chapter, new techniques are presented for two-port device de-embedding on actual

GCPW measurement data. The results of modeling, simulation and measurements are in good agreement.

3.2 Analytical Study of the GCPW

General CPW structures were studied by the FEM in the 1990s [44]. In this section, analytical expressions of conductor loss and dielectric loss are provided. They are either from conformal mapping, quasi-static and/or full-wave solution, or extracted from experimental date.

3.2.1 Coplanar Waveguide Structures and Dimension

The cross-section and top view of the GCPW is shown in Fig. 20 and Fig. 21, respectively. The GCPW is connected to WR-12 waveguide at its two ends. There is a connector plate at each of these connection which introduce an offset length
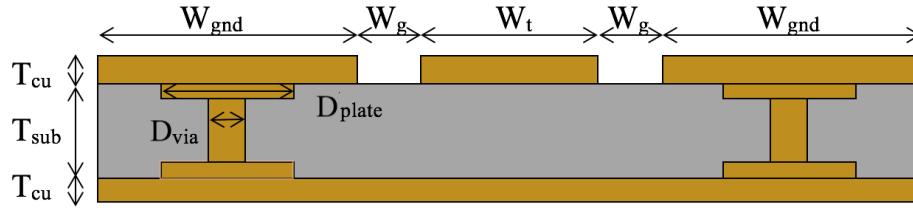

Figure 20. Cross-section of Coplanar Waveguide

with dimensions listed in Table 5.

In our study, the PCB board was Parasonic Magnon7, high speed, low loss multi-layer materials. The center trace and ground planes are made of copper, and dielectric
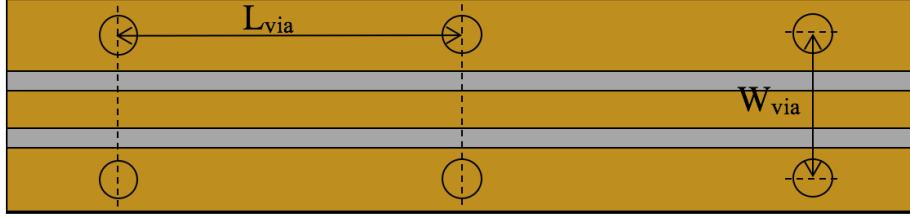
Figure 21. Top View of Coplanar Waveguide

Table 5. Parameters

Dimension of	Length
W_t–Trace width	$262\mu m$
W_g–Gap width	$77\mu m$
W_{gnd}–Lateral ground plane width	$1.584mm$
T_{sub}–Substrate thickness	$130\mu m$
T_{Cu}–Copper thickness	$30\mu m$
D_{plate}–Diameter of plate	$250\mu m$
D_{via}–Diameter of via conductor	$100\mu m$
W_{via}–Vertical via conductor separation	$1mm$
L_{via}– Horizontal via conductor separation	$300\mu m$

substrate has relative permittivity of 3.2 and loss tangent of 0.004 at 50 GHz in the data sheets.

3.2.2 Analytical Solution of Attenuation for GCPW

The total attenuation consists of two parts, the conductor loss and dielectric loss. The conductor loss due to skin effect is proportional to the square-root of frequency, while the dielectic loss (contantance) grows faster than a linear function of frequency [44]. Therefore at E-band frequencies dielectric loss is dominant.

3.2.3 Conductor Loss

From [45], the conductor loss of GCPW is

$$\alpha_c = \frac{R_s\sqrt{\varepsilon_{eff}}}{480\pi K(k_1)K'(k_1)(1-k_1^2)}$$
$$\times \left\{\frac{1}{a}\left[\pi + \ln\frac{8\pi a(1-k_1)}{t(1+k_1)}\right] + \frac{1}{b}\left[\pi + \ln\frac{8\pi b(1-k_1)}{t(1+k_1)}\right]\right\} \quad \text{[Np/m]} \quad (3.1)$$

where

$$a = W_t/2, b = W_t/2 + W_g$$

$$\varepsilon_{eff} = 1 + q(\varepsilon_r - 1)$$

$$q = \frac{\frac{K(k_3)}{K'(k_3)}}{\frac{K(k_1)}{K'(k_1)} + \frac{K(k_3)}{K'(k_3)}}$$

$$k_1 = a/b$$

$$k_3 = \frac{\tanh\frac{\pi W_t}{4T_{sub}}}{\tanh\frac{\pi(W_t+2W_g)}{4T_{sub}}}$$

$$R_s = \sqrt{\frac{\omega\mu_0\mu_r}{2\sigma}}$$

σ is the conductivity of the conductor. K and K' are elliptic integral of the first kind and its complement.

In practice, if roughness is considered, the conduction loss α_c' becomes [46]

$$\alpha_c' = \alpha_c\left[1 + \frac{2}{\pi}\tan^{-1}1.4\left(\frac{\Delta}{\delta_S}\right)^2\right] \tag{3.2}$$

3.2.4 Dielectric Loss

The dielectric loss of GCPW is the same as microstrip line case as stated in [46]

$$\alpha_d = \frac{k_0\varepsilon_r(\varepsilon_{eff}-1)\tan\delta}{2\sqrt{\varepsilon_{eff}}(\varepsilon_r-1)} \quad \text{[Np/m]} \tag{3.3}$$

where k_0 is the free space propagation constant. The total attenuation therefore is simply sum of conduction and dielectric loss $\alpha_{tot} = \alpha_c + \alpha_d$.

3.2.5   Characteristic Impedance

The characteristic impedance of GCPW is given in [47]

$$Z_0 = \frac{60\pi}{\sqrt{\varepsilon_{eff}}} \frac{1}{\frac{K(k_1)}{K(k_1')} + \frac{K(k_l)}{K(k_l')}} \tag{3.4}$$

where

$$k_1' = \sqrt{1 - k_1^2}$$
$$k_l = \frac{\tanh\left(\frac{\pi a}{2h}\right)}{\tanh\left(\frac{\pi b}{2h}\right)}$$
$$k_l' = \sqrt{1 - k_l^2}$$

Therefore the characteristic impedance of the GCPW is 50.01Ω which is good for any 50Ω system.

3.3   Simulation Results

Compared analytic solution with simulation is in Fig. 22.

It shows good match between analytic solution to HFSS simulation. At low frequency, the conductor loss is dominant and is proportional to square root of frequency. At higher frequency, the dielectric loss is dominant and therefore has linear relationship to frequency.
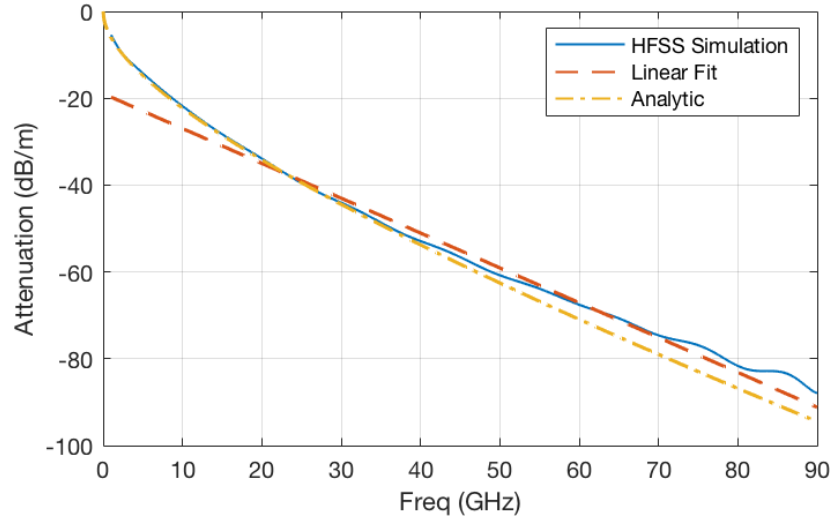
Figure 22. Attenuation of GCPW from Analytic Solution, HFSS Simulation, and Linear Fit

3.4 Measurements and Calibration

Due to device connection misalignment, addition calibrations are needed to find true S-parameters for the DUT with one- and/or two- port. The misalignment in measurement can be modeled as two error S-matrices with one before DUT and the other after DUT. To solve the unknown error S-matrices, use both one-port and two-port with offset shorts and throughs for calibration.

3.4.1 One-port Calibration

One-port device with error box is shown in Fig. 23, and our goal is to find S_{11} following steps in [48].

47
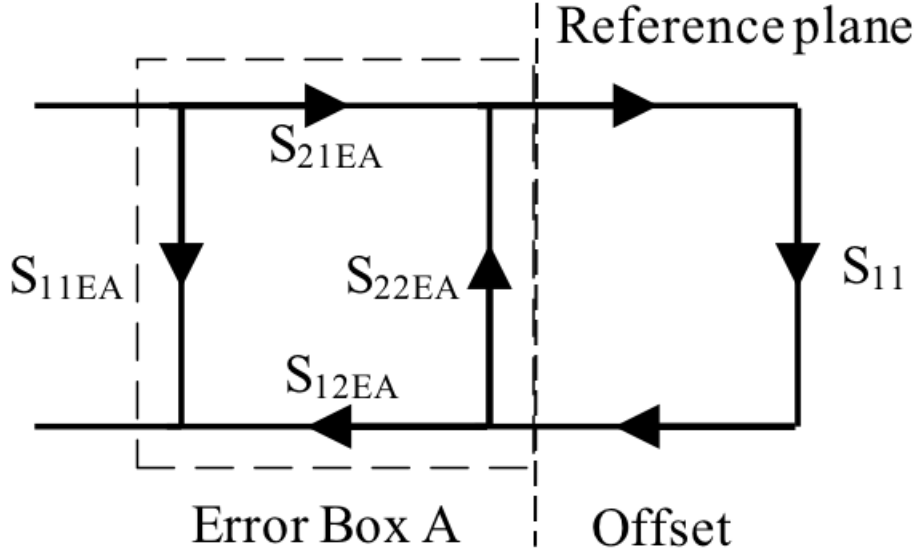
Figure 23. Schematics of One-port Device with Embedded Error Box

The true S_{11} of the DUT is

$$S_{11} = S_{11EA} + \frac{S_{12EA}S_{21EA}S_{11}}{1 - S_{22EA}S_{11}} \tag{3.5}$$

where S_{EA} represents S-parameters of the embedded error box, and S_{11} is of the DUT.

In order to de-embed error box, use a standard short component and with at least three different offset shorts to determine the three unknowns S_{11EA}, $S_{12EA}S_{21EA}$, and S_{22EA}.

3.4.2 Two-port Calibration

Two-port devices (Fig. 24) require more calibration work. Assuming that the DUT is reciprocal (no active devices or ferrites) such that $S_{21} = S_{12}$, and no reflection from error boxes, namely $S_{11EA} = S_{22EB} = 0$. Use VNA that is one-path propagation only from port one to port two. Then safely assume $S_{12EA} = S_{12EB} = 0$ since they are irrelevant to measured S_{21}.
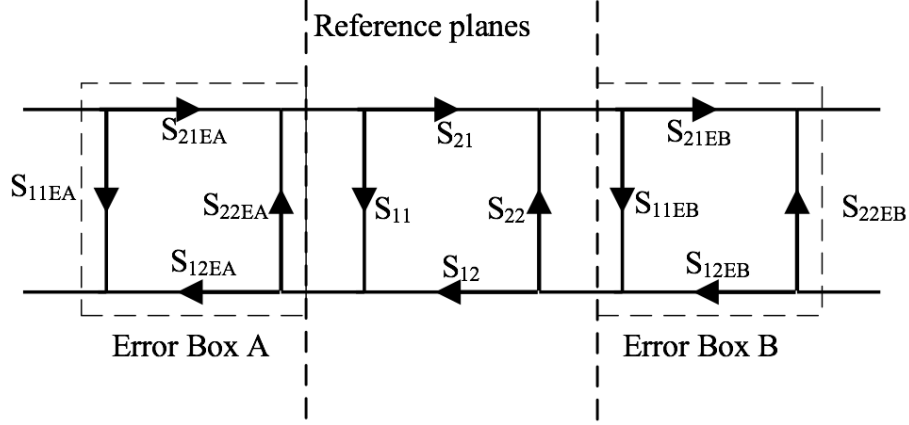
Figure 24. Schematics of Two-port Device with Embedded Error Box

To solve the cascade system, it is easier to use transfer matrix instead of S-parameters. The conversion of T-matrix from S-matrix is

$$[T] = \frac{1}{S_{21}} \begin{bmatrix} S_{12}S_{21} - S_{11}S_{22} & S_{11} \\ -S_{22} & 1 \end{bmatrix} \quad (3.6)$$

Then the total T-matrix is the product all three T-matrixes

$$[T_m] = \frac{1}{S_{21\mathrm{m}}} \begin{bmatrix} S_{12m}S_{21\mathrm{m}} - S_{11m}S_{22m} & S_{11m} \\ -S_{22m} & 1 \end{bmatrix}$$

$$= \frac{1}{S_{21EA}S_{21}S_{21EB}} \times$$

$$\begin{bmatrix} 0 & 0 \\ 0 & -S_{11EB}[S_{22EA}(S_{21}^2 - S_{11}^2) + S_{11}] - S_{22EA}S_{11} + 1 \end{bmatrix} \quad (3.7)$$

where S_m represents measured S-parameter. Rearrange equation (3.7) and get a quadratic equation for S_{21}

$$S_{11EB}S_{22EA}S_{21\mathrm{m}}S_{21}^2 + S_{21EA}S_{21EB}S_{21} -$$

$$S_{21\mathrm{m}}S_{11EB}S_{22EA}S_{11}^2 + S_{21\mathrm{m}}S_{11EB}S_{11} - S_{21\mathrm{m}} = 0 \quad (3.8)$$

49

Then pick one root when solving the quadratic equation. The physical answer should be close to the value before calibration and below 0 dB. Next, use different length of offsets as DUT. If the length of the offset is l and short distance, then its T-matrix simply be

$$[T_{off}] = \begin{bmatrix} e^{-j\beta l} & 0 \\ 0 & e^{j\beta l} \end{bmatrix} \tag{3.9}$$

where β represents propagation constant inside the offset waveguide. Substituting (3.9) into (3.7) and rearrange terms to get

$$S_{21\mathrm{m}}e^{-j2\beta l}S_{11EB}S_{22EA} + e^{-j\beta l}S_{21EA}S_{21EB} = S_{21\mathrm{m}} \tag{3.10}$$

Solve for $S_{11EB}S_{22EA}$ and $S_{21EA}S_{21EB}$ with at least two different offsets. The propagation constant, β, can be derived from rectangular waveguide formula.

Next, S_{22EA} can be found from one-port calibration in the previous session. And $S_{11EB} = S_{11EB}S_{22EA}/S_{22EA}$. Now all parameters are known for solving the quadratic equation of true S_{21}.

3.4.3   Measurement Results

The Rohde & ShwarzS ZVA24 VNA and V10VNA2 frequency extender are employed so that frequency range can go from 75 GHz to 110 GHz. The measured GCPW is 45mm long operating from 75-84 GHz. The measurement results are compared with analytic solution and HFSS simulation, showning in Fig. 25. We assume maximum roughness when calculate analytic solution. In specific, conduction loss in (3.2) becomes $\alpha'_c = 2\alpha_c$.
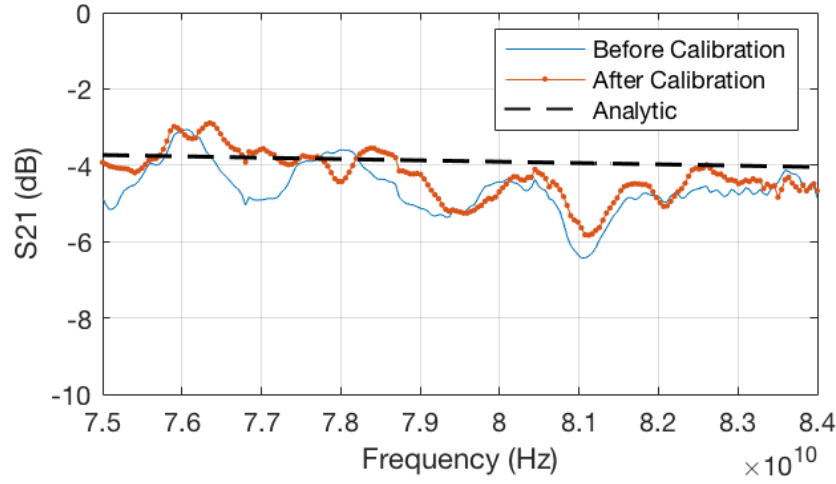
Figure 25. Comparison of GCPW Attenuation Between Analytic Solution, Measurement with and without Calibration

3.5 Summary

In this application oriented chapter, we summarized analytical expressions of Ohmic loss, dielectric loss and attenuation of the GCPW at the E-band frequency range. Using commercial EM simulation package, HFSS, to execute frequency-sweeping simulations. Then use Rohde & ShwarzS ZVA24 VNA and V10VNA2 frequency extender for measurement from 75GHz to 84GHz. Device misalignment becomes prominent under millimeter wavelength range which requires additional calibration of the system. By using offsets short and through as DUTs, S-matrices due to misalignment are calculated for all frequency range, and can be de-embedded to retrieve true S-parameters. Finally the measured date is compared with analytic modeling results and HFSS simulation outputs and good agreement is observed. The model can be used for other applications such as system and circuit design, and for device tuneup.

Chapter 4

E-BAND 3-D PRINTED ANTENNA FABRICATION AND MEASUREMENT
USING VNA AND ONE-SIDE FREQUENCY-EXTENDER

4.1 Introduction

While most affordable microwave vector network analyzers (VNAs) covers only Ku, K and Ka bands, automotive radars use the millimeter wave E-band or W-band frequencies, typically 75-81 GHz. For instance, the HP-8720 has its upper limit of 16 GHz, Rohde ZVA24 goes to 24 GHz, and Agilent 8510C goes to 40 GHz. To make a full two-port measurement, one will need to have a pair of frequency-extenders, e.g., from the OML or other vendors. To reduce the burden of equipment budget, use a single frequency-extender and conduct a half two-port test, measuring S11 and S21. Then use reciprocity principle to estimate S_{12}. In such a way the extension budget may have been cut in a half. The extender utilizes a specific RF signal from the VNA for its harmonics. As a result, HP8720 and any VNA below 20 GHz may be difficult for extension.

The basic calibration procedures are as follows. First, one needs to do the one-port calibration for Port 1 by placing Short, Offset-short, Match and Sliding match (optional). Then connect Port 2 with Through and Isolation. More detailed discussions can be found in the previous chapter. This chapter emphasizes on one-port offset correction, using the Smith chart [49].

For the radar system, antennas are pyramidal horns and cavity backed slotted

arrays using substrate integrated waveguide (SIW). For simplicity, only the 3D printed plastic horn will be reported.
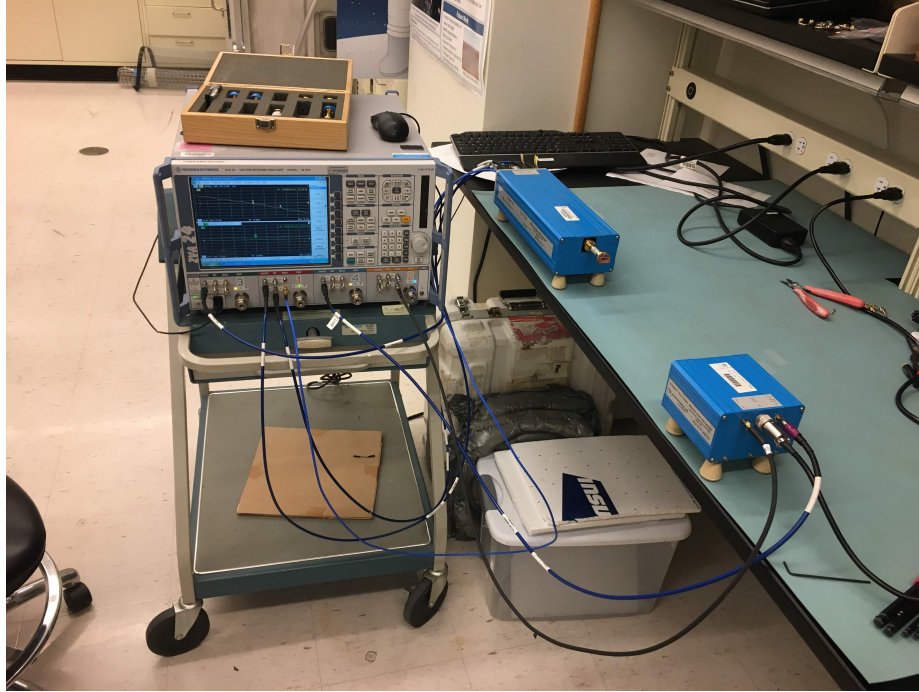

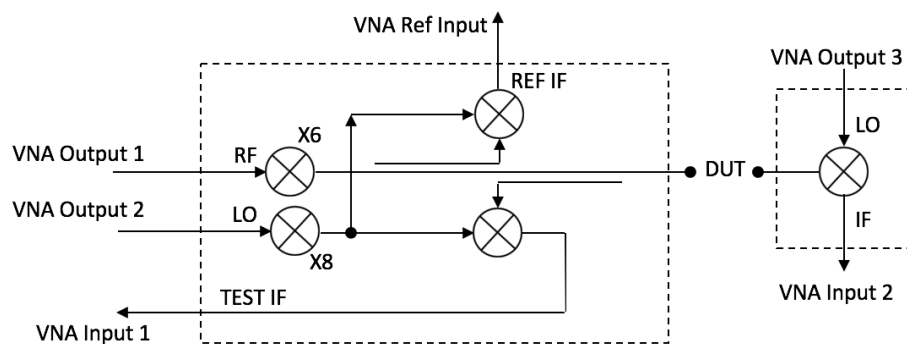Figure 26. ROHDE&SCHWARZ ZVA24 Connected to the Extenders at Lab Measurement

Figure 27. Block Diagram of OML V10VNA2 Extenders and Connection Setup to VNA

4.2 Equipment Setup

Using the VNA of Rohde & Schwarz ZVA24, with frequency range from 10 MHz to 24 GHz, cnnects this VNA to the extender of Olson Microwave Lab (OML) V10VNA2-T/R at Port-1 for transmitting and receiving, and V10VNA2-R at another port for receiving only. Because the extender at one port is only for receiving, only one-path signal can be measured. To have full two-path measurement, both V10VNA2-T/R extenders are required. The photo of extenders are shown in Fig. 26. Its block diagram and connection are illustrated in Fig. 27.

According to the block diagram, the extender is a superheterodyne that shifts RF signal of 12.5-18.33 GHz to 75-110 GHz and then the mm-waves pass through DUT. The reflected and transmitted signals are mixed with up-shifted LO of 74.72GHz-109.72GHz, resulting in IF at 280 MHz which is measurable by the VNA.

It is worth noting that the VNA built-in direct coupler (shown in Fig. 28) is troublesome when directly connecting to the extender. It makes measurement results extremely noisy and inaccurate (even after 16 times average), especially in 79.5-84.0 GHz frequency range. As the result, bypassing the coupler by connecting the source port on VNA to the extender directly, much cleaner signals are observed in calibration and measurement. One possible explanation might be the phase noise due to the coupler in VNA, which contaminated frequency multiplier in the extender.

4.3 Horn Antenna versus Micro-strip Antenna

Micro-strip antenna has low profile and is conformable to plane and curved surfaces. Mechanically micro-strip is robust on rigid surface, and ease to produce by the printed
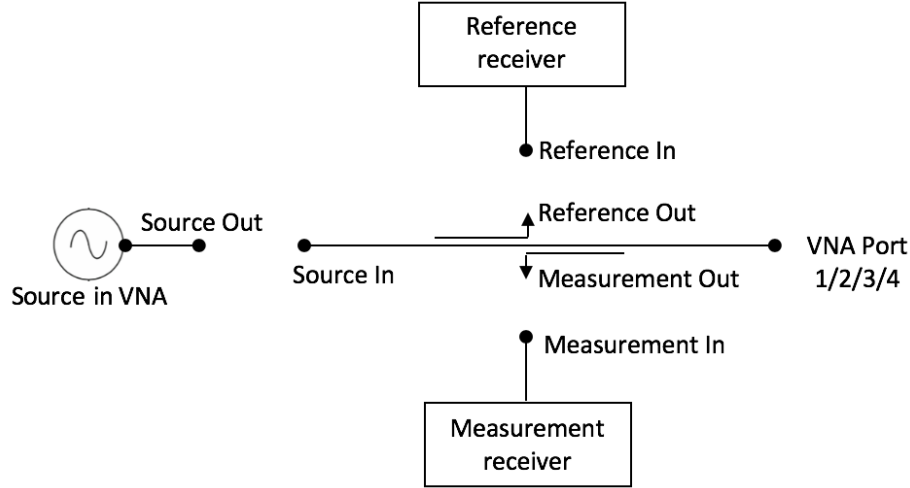
Figure 28. ROHDE&SCHWARZ ZVA24 Built-in Coupler Block Diagram

circuit board (PCB) technology in Low cost. These antennas are compatible to the MMIC design and fabrication. They are versatile in resonance frequency, pattern, impedance and polarization by adding pins and varactor diodes between the patches and ground plane. However, micro-strip antennas have low efficiency, low power and high Q. They are poor in polarization purity, and may produce spurious feeding radiation.

On the contrary, horn antennas have large gain and high radiation efficiency, with high polarization purity. Due to their versatility and overall performance, Horns are the simplest and widely used microwave antennas. In this talk, the designed antenna is a pyramidal horn with WR-12 rectangular waveguide as the feeding terminal, as shown in Fig. 29. Both antenna and flange are integrated together and can be easily produced by 3D printing. Due to 3D printer finite resolution of $\pm 100\mu$, the interior walls of horn show step rings. This roughness may slightly degrade antenna gain and insertion loss.

The 3D printed horn antennas are plastic, using conventional ABS material which
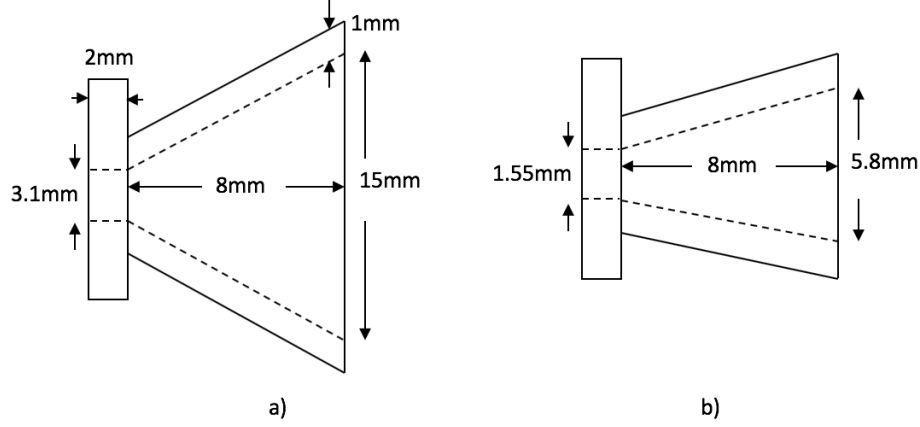
Figure 29. Copper Electroplated Horn Antennas with WR-12 Connector: (a) Top View. (b) Side View.

is non-conducting. Then coated the horns with copper in the lab. There are many ways to do electroplating. Graphite-acetone mixture was utilized for base conducting plane because acetone can etch ABS material so that graphite will stick onto the ABS surface. After waiting 24 hours for acetone to dry completely, dipped the horns into copper sulphate solution and ready for electroplating. Then connect the horn to cathode and copper wire to anode, both dipped completely in the electrolyte. The power source is 7V DC home adapter. The electroplating process took about 10 hours for each horn antenna. Photo of some finished horn antennas integrated with standard W-band flanges are shown in Fig. (30).

In [50], the horn antenna directivity is giving as

$$
\begin{aligned}
D = &\frac{8\pi\rho_1\rho_2}{a_1 b_1}\{[C(u) - C(v)]^2 + [S(u) - S(v)]^2\} \\
&\times \left\{C^2\left(\frac{b_1}{\sqrt{2\lambda\rho_1}}\right) + S^2\left(\frac{b_1}{\sqrt{2\lambda\rho_1}}\right)\right\}
\end{aligned} \tag{4.1}
$$

where some parameters are

C and S represents Fresnel cosine and sine integral functions, respectively. The
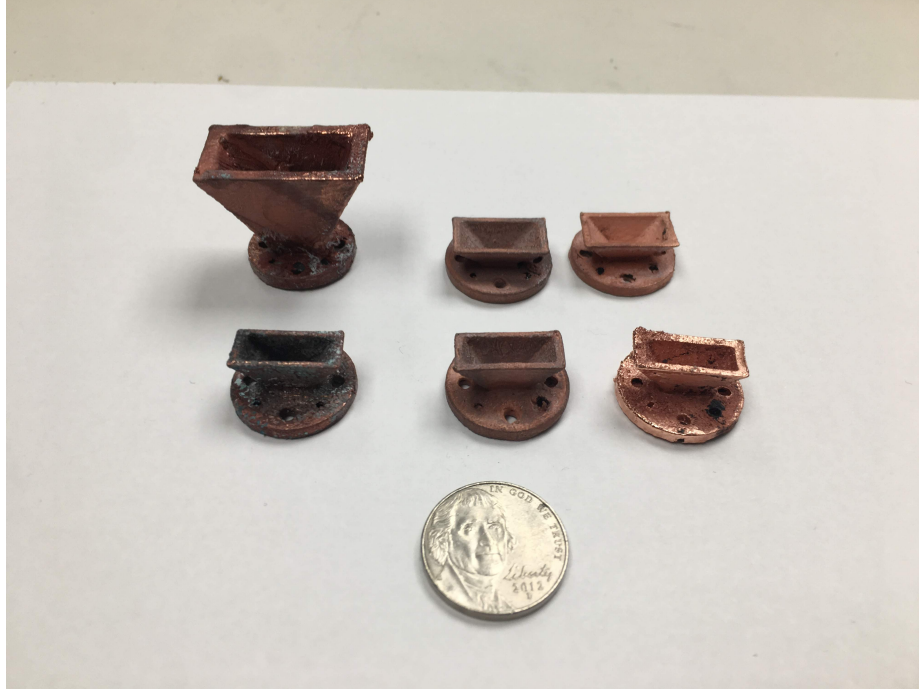
Figure 30. Copper Electroplated Horn Antennas with WR-12 Connector

Parameters	Values
a_1	$15mm$
b_1	$5.8mm$
a	$3.1mm$
b	$1.55mm$
ρ_1	$10.9mm$
ρ_2	$10.1mm$

antenna pattern is shown in Fig. 31. At 76.5GHz, the E-plane half power beam width (HPBW) is about $\pm 17°$ and H-plane HPBW is $\pm 15°$.

4.4 Antenna Measurement

For the measurement, connected one pair of same horn antennas to the transmitting frequency-extender and receiving frequency-extender covered with absorber material,
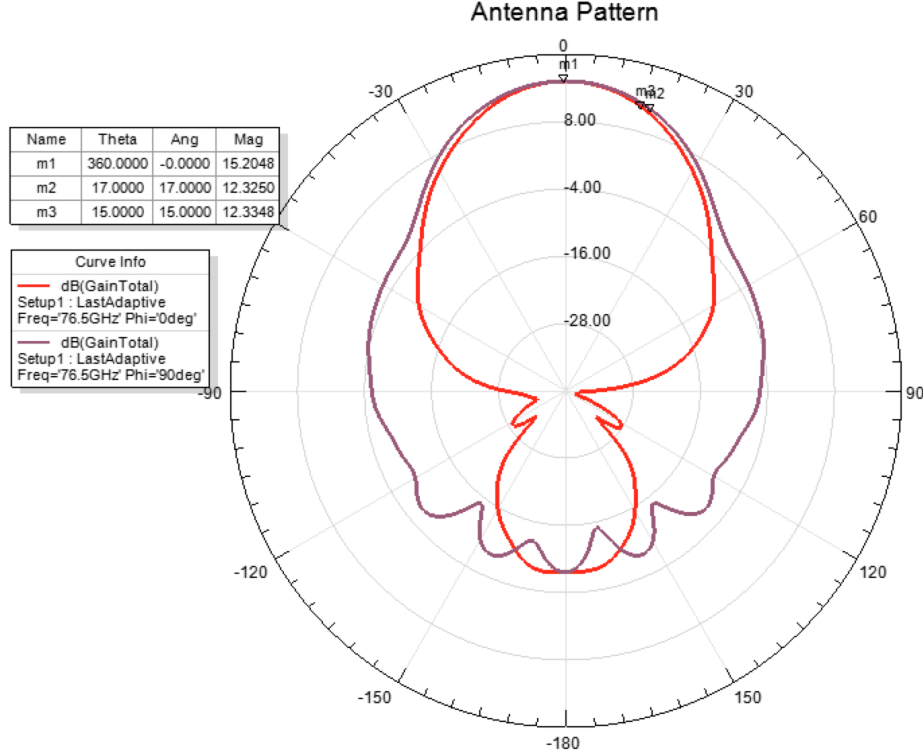
Figure 31. Antenna Patter of E-Plane ($\phi = 90°$) and H-Plane ($\phi = 0°$)

SB-1007-040, 1.0 mm thick, (20-110 GHz). Two antennas were separated by 67cm to ensure the far zone condition. Figure 32 demonstrates the recorded raw data of magnitude for S11 and S21 in frequency range of 75-78 GHz, which are used to calculate the antenna gain below.

Employing the Friis transmission equation and assume the transmitting and receiving antennas are identical

$$Gain = \sqrt{\left(\frac{4\pi R}{\lambda}\right)^2 \frac{S_{21}^2}{1 - S_{11}^2}} \tag{4.2}$$

The insertion loss and gain are presented in Fig. 33 and Fig. 34, both compared to HFSS simulation and analytic values. Due to presented surface roughness and fabrication variance, there is some difference between measurement and simulated values.
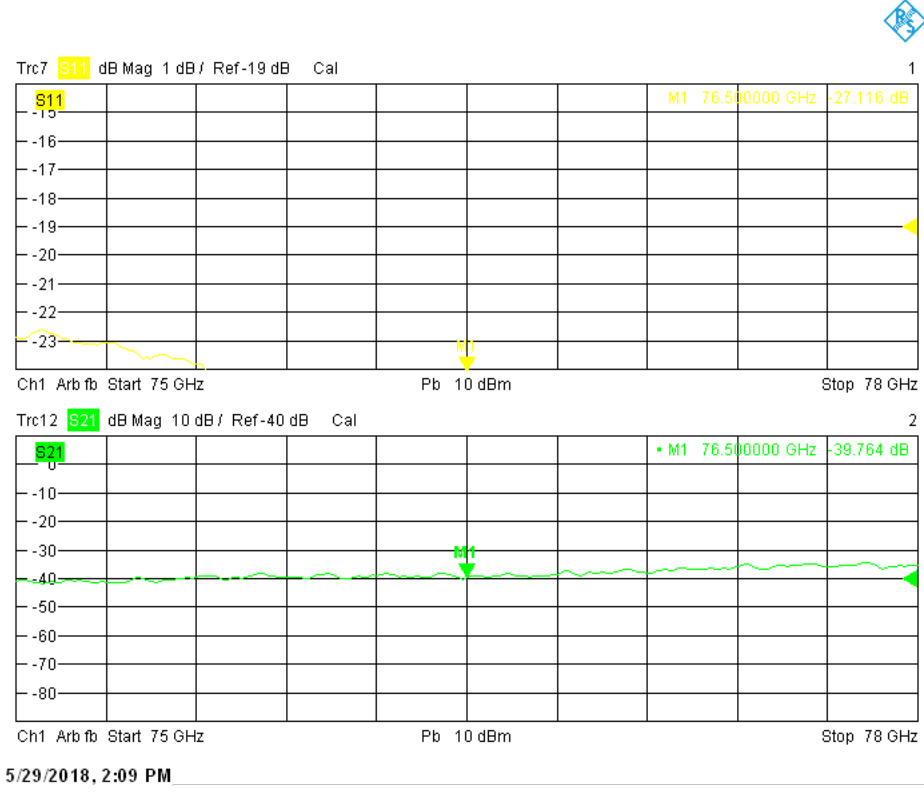
Figure 32. Measured magnitude of S11 and S21 versus frequency

4.5   Summary

This chapter shows the possibility of 3D printed horn antenna working in 75GHz to 78GHz. The 3D printing and electroplating process is low cost and time-efficient in fabrication and yet not much degrade from analytic and simulation results in antenna gain at E-band. Similar process could also work for other type of antenna in the future for low cost, small, and irregular antennas.

59

Figure 33. Comparison of HFSS Simulated and Measurement Insertion Loss

Figure 34. Comparison of HFSS Simulated, Measurement and Analytic Solution of Antenna Gain

REFERENCES

[1] L. J. Chu, "Physical limitations of omni-directional antennas," *J. Appl. Phys.*, vol. 19, pp. 1163–1175, 1948.

[2] H. A. Wheeler, "The radiansphere around a small antenna," *Proc. IRE*, vol. 47, pp. 1325–1331, 1959.

[3] R. F. Harrington, "Effects of antenna size on gain, bandwidth, and efficiency," *Journal National Bureau of Standards*, vol. 64-D, pp. 1–12, 1960.
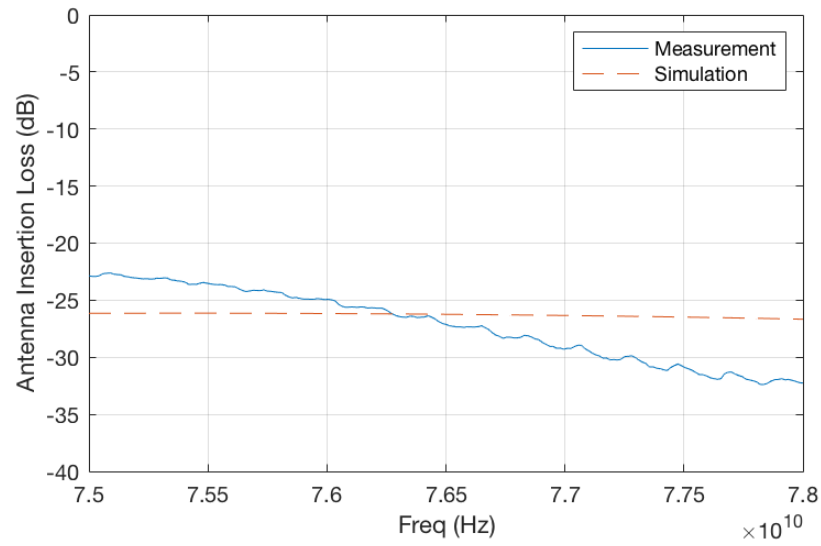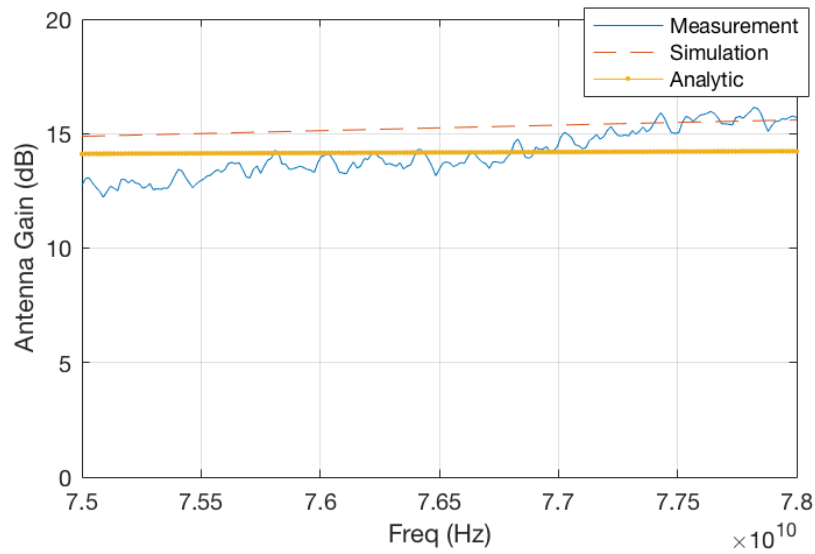
[4] R. C. Hansen and R. E. Collin, "A new chu formula for q," *IEEE Antennas Propag. Mag.*, vol. 51, pp. 38–41, 2009.

[5] M. Gustafsson, C. Sohl, and G. Kristensson, "Illustrations of new physical bounds on linearly polarized antennas," *IEEE Transactions on Antennas and Propagation*, vol. 57, no. 5, pp. 1319–1327, 2009. DOI: 10.1109/TAP.2009.2016683.

[6] B. D. Popovic, "Theory of cylindrical antennas in conducting media," in *Institution of Electrical Engineers*, vol. 118, 1971, pp. 507–510.

[7] T. J. Cui and W. C. Chew, "Accurate model of arbitrary wire antennas in free space, above or inside ground," *IEEE Trans. Antennas Propagat.*, vol. 48, pp. 482–493, 2000.

[8] R. K. Moore and W. E. Blair, "Dipole radiation in a conducting half space," *Journal of research of the National Bureau of Standards-D. Radio Propagation*, vol. 65D, no. 6, pp. 547–563, 1961.

[9] C. Guclu, S. Campione, and F. Capolino, "Array of dipoles near a hyperbolic metamaterial: Evanescent-to-propagating floquet wave transformation," *Phys. Rev. B*, vol. 89, p. 155 128, 15 2014. DOI: 10.1103/PhysRevB.89.155128. [Online]. Available: https://link.aps.org/doi/10.1103/PhysRevB.89.155128.

[10] C. Valagiannopoulos, "An overview of the watson transformation presented through a simple example," *Progress in Electromagnetics Research-pier - PROG ELECTROMAGN RES*, pp. 137–152, Aug. 2007. DOI: 10.2528/PIER07052502.

[11] L. Zhang and G. G. Pan, "Fast coiflet magnetic field integral equation for scattering from open rough surfaces," *IET Microwaves, Antennas Propagation*, vol. 10, no. 8, pp. 836–842, 2016.

[12] G. Pan, *Wavelets in Electromagnetics and Device Modeling*. John Wiley and Sons, Inc., 2003.

[13] S. Zhou, G. Pan, K. Zhang, C. Pan, and C. Davis, "E-band 3-d printed antenna fabrication and measurement using vna and one-side frequency-extender," in *2018 IEEE 27th Conference on Electrical Performance of Electronic Packaging and Systems EPEPS*, 2018, pp. 127–129.

[14] O. D. Miller, A. G. Polimeridis, M. T. H. Reid, *et al.*, "Fundamental limits to optical response in absorptive systems," *Opt. Express*, vol. 24, no. 4, pp. 3329–3364, 2016. DOI: 10.1364/OE.24.003329. [Online]. Available: http://www.opticsexpress.org/abstract.cfm?URI=oe-24-4-3329.

[15] A. Sheverdin and C. Valagiannopoulos, "Core-shell nanospheres under visible light: Optimal absorption, scattering, and cloaking," *Physical Review B*, vol. 99, Feb. 2019. DOI: 10.1103/PhysRevB.99.075305.

[16] A. Abrashuly and C. Valagiannopoulos, "Limits for absorption and scattering by core-shell nanowires in the visible spectrum," *Phys. Rev. Applied*, vol. 11, p. 014 051, 1 2019. DOI: 10.1103/PhysRevApplied.11.014051. [Online]. Available: https://link.aps.org/doi/10.1103/PhysRevApplied.11.014051.

[17] R. E. Diaz and T. Sebastian, "Electromagnetic limits to radiofrequency (rf) neuronal telemetry," *Scientific Reports*, vol. 3, no. 1, p. 3535, 2013. DOI: 10.1038/srep03535. [Online]. Available: https://doi.org/10.1038/srep03535.

[18] T. Olsson, *A mechanically based antenna (ameba)*, DARPA, Microsystem Technology Office, 2017. [Online]. Available: https://beta.sam.gov/opp/a7ad32588088d94cf6d66af19851b22e/view.

[19] J. A. Stratton, "Electromagnetic theory," in New York: McGraw-Hill Book Company, 1941, ch. VII, pp. 392–393.

[20] D. K. Cheng, *Field and wave Electromagnetics*. Boston, Massachusetts: Addison-Wesley, 1992.

[21] C. A. Valagiannopoulos and A. Alú, "The role of reactive energy in the radiation by a dipole antenna," *IEEE Transactions on Antennas and Propagation*, vol. 63, no. 8, pp. 3736–3741, 2015. DOI: 10.1109/TAP.2015.2436410.

[22] G. Pan and S. Zhou, "Multi-physics generated small dipoles in lossy media," in *IEEE International Symposium on Antennas and Propagation and USNC-*

URSI Radio Science, Institute of Electrical and Electronics Engineers Inc., 2018, pp. 61–62.

[23] D. Miron, "A study of the ctha based on analytical models," *IEEE Trans. Ant. Prop.*, vol. 49, pp. 1130–1137, 2001.

[24] R. Hansen and R. Ridgley, "Fields of the contrawound toroidal helix antenna," *IEEE Trans. Ant. Prop.*, vol. 49, pp. 1138–44, 2001.

[25] K. McDonald, *Radiation in the near zone of a small loop antenna*, 2004. [Online]. Available: http://puhep1.princeton.edu/~mcdonald/examples/smallloop.pdf.

[26] M. Manteghi and A. A. Y. Ibraheem, "On the study of the near-fields of electric and magnetic small antennas in lossy media," *IEEE Trans. Antennas Propagat.*, vol. 62, pp. 6491–6495, 2014.

[27] J. Griffith and G. Pan, "Time harmonic fields produced by circular current loops," *IEEE Trans. Magnetics*, vol. 47, pp. 2029–2033, 2011.

[28] T. Yousefi, T. Sebastian, and R. E. Diaz, "Why the magnetic loss tangent is not a relevant constraint for permeable conformal antennas," *IEEE Trans. Magnetics*, vol. 64, pp. 2784–2796, 2016.

[29] J. Itoh *et al.*, "Development of high efficiency flywheel energy storage system for power load-leveling," in *2014 IEEE 36th International Telecommunications Energy Conference (INTELEC)*, 2014, pp. 1–8.

[30] H. C. Burch, A. Garraud, M. F. Mitchell, R. C. Moore, and D. P. Arnold, "Experimental generation of elf radio signals using a rotating magnet," *IEEE Transactions on Antennas and Propagation*, vol. 66, no. 11, pp. 6265–6272, 2018. DOI: 10.1109/TAP.2018.2869205.

[31] M. Gołkowski, J. Park, J. Bittle, B. Babaiahgari, R. A. L. Rorrer, and Z. Celinski, "Novel mechanical magnetic shutter antenna for elf /vlf radiation," in *2018 IEEE International Symposium on Antennas and Propagation USNC/URSI National Radio Science Meeting*, 2018, pp. 65–66. DOI: 10.1109/APUSNCURSINRSM. 2018.8608677.

[32] H. G. Schantz, "Electromagnetic energy around hertzian dipoles," *IEEE Antennas and Propagation Magazine*, vol. 43, no. 2, pp. 50–62, 2001. DOI: 10.1109/74. 924604.

[33] S. H. Schot, "Eighty years of sommerfeld's radiation condition," *Historia Mathematica*, vol. 19, pp. 385–401, 1992.

[34] O. Heaviside, *Electromagnetic Theory Volume III*. London: The Electrician Print. and Pub. Co., 1912.

[35] S. A. Schelkunoff and H. T. Friis, *Antennas : theory and practice*. New York: J. Wiley, 1952.

[36] P. Carter, "Circuit relations in radiating systems and applications to antenna problems," *Proceedings of the Institute of Radio Engineers*, vol. 20, no. 6, pp. 1004–1041, 1932. DOI: 10.1109/JRPROC.1932.227723.

[37] R. Harrington, "Matrix methods for field problems," *Proceedings of the IEEE*, vol. 55, no. 2, pp. 136–149, 1967. DOI: 10.1109/PROC.1967.5433.

[38] V. Barrera-Figueroa, J. Sosa-Pedroza, and J. L. López-Bonilla, "Simplification of pocklington's integral equation for arbitrary bent thin wires," 2005.

[39] B. Acharjee and M. A. Matin, "Analysis of wire antennas by solving pocklington's integral equation using wavelets," in *2008 International Conference on Electrical and Computer Engineering*, 2008, pp. 778–782. DOI: 10.1109/ICECE.2008.4769315.

[40] J. E. Storer, "Impedance of thin-wire loop antennas," *Transactions of the American Institute of Electrical Engineers, Part I: Communication and Electronics*, vol. 75, no. 5, pp. 606–619, 1956. DOI: 10.1109/TCE.1956.6372437.

[41] K. Awadalla and A.-E.-M. Sharshar, "A simple method to determine the impedance of a loop antenna," *IEEE Transactions on Antennas and Propagation*, vol. 32, no. 11, pp. 1248–1251, 1984. DOI: 10.1109/TAP.1984.1143237.

[42] R. E. Collin, *Antennas and radiowave propagation*. New York: McGraw-Hill, 1985.

[43] A. U. Zaman, V. Vassilev, P.-S. Kildal, and H. Zirath, "Millimeter wave e-plane transition from waveguide to microstrip line with large substrate size related to mmic integration," *IEEE Microwave and Wireless Components Letters*, vol. 26, no. 7, pp. 481–483, 2016. DOI: 10.1109/LMWC.2016.2574995.

[44] G. Pan and J. Tan, "General edge element approach to lossy and dispersive structures in anisotropic media," English, *IEE Proceedings - Microwaves, An-*

tennas and Propagation, vol. 144, 81–90(9), 2 1997. [Online]. Available: https://digital-library.theiet.org/content/journals/10.1049/ip-map_19970507.

[45] G. Ghione, "A cad-oriented analytical model for the losses of general asymmetric coplanar lines in hybrid and monolithic mics," *IEEE Transactions on Microwave Theory and Techniques*, vol. 41, no. 9, pp. 1499–1510, 1993. DOI: 10.1109/22.245668.

[46] D. M. Pozar, *Microwave Engineering*. NJ: Wiley, 2011.

[47] B. C. Wadell, "Transmission line design handbook," in 4. Boston, Massachusetts: Artech House, 1991, ch. 3, p. 79.

[48] W. Sigg and J. Simon, "Reflectometer calibration using load, short and offset shorts with unknown phase," English, *Electronics Letters*, vol. 27, 1650–1651(1), 18 1991. [Online]. Available: https://digital-library.theiet.org/content/journals/10.1049/el_19911031.

[49] Z. Liu and R. Weikle, "A reflectometer calibration method resistant to waveguide flange misalignment," *IEEE Transactions on Microwave Theory and Techniques*, vol. 54, no. 6, pp. 2447–2452, 2006. DOI: 10.1109/TMTT.2006.875795.

[50] J. Kraus, R. Marhefka, and A. Khan, *Antennas and Wave Propagation*, ser. McGraw-Hill series in electrical engineering. McGraw-Hill, 2017.

APPENDIX A

POWER CALCULATIONS FOR TM AND TE CASES

The total power density along radial direction of TM mode is

$$W_r = E_\theta H_\phi^* = \eta \left(\frac{I_e dl}{4\pi} |k| \right)^2 \left(\frac{1}{r} + \frac{1}{jkr^2} - \frac{1}{k^2 r^3} \right)$$
$$\times \left(\frac{1}{r} + \frac{1}{jkr^2} \right)^* \sin^2 \theta e^{-2\alpha r} \tag{A.1}$$

Then integrate over close spherical surface to get total power flowing from the dipole

$$S_{TM} = \frac{1}{2} \text{Re} \int_0^{2\pi} \int_0^\pi W_r r^2 \sin\theta d\theta d\phi$$
$$= \frac{1}{2} \left(\frac{I_e dl}{4\pi} |k| \right) e^{-2\alpha r} (2\pi) \frac{4}{3} \text{Re} \left[\eta \left(1 + \frac{1}{jkr} \right. \right.$$
$$\left. \left. - \frac{1}{jk^* r} + \frac{1}{|k|^2 r^2} - \frac{1}{k^2 r^2} + \frac{1}{j|k|^2 k^3} \right) \right] \tag{A.2}$$

Substituting

$$\eta = \frac{\eta_0 \omega}{|k|^2 c} (\beta + j\alpha)$$

and after some manipulation

$$S_{TM} = \frac{1}{12\pi} (I_e dl)^2 \frac{\eta_0 \omega}{c} e^{-2\alpha r} \beta \left[1 + \frac{2\alpha}{|k|^2 r} + \frac{1}{|k|^2 r^2} \right.$$
$$\left. - \frac{\beta^2 - 3\alpha^2}{|k|^4 r^2} + \frac{2\alpha}{|k|^4 r^3} \right] \tag{A.3}$$

Similarly for TE case

$$W_r = E_\phi H_\theta^* = -\frac{1}{\eta^*} \left(\frac{I_m dl}{4\pi} |k| \right)^2 \left(\frac{1}{r} + \frac{1}{jkr^2} - \frac{1}{k^2 r^3} \right)^*$$
$$\times \left(\frac{1}{r} + \frac{1}{jkr^2} \right) \sin^2 \theta e^{-2\alpha r} \tag{A.4}$$

Total power is

$$S_{TM} = \frac{1}{2} \left(\frac{I_m dl}{4\pi} |k| \right) e^{-2\alpha r} (2\pi) \frac{4}{3} \text{Re} \left[\frac{1}{\eta^*} \left(1 + \frac{1}{jkr} \right. \right.$$
$$\left. \left. - \frac{1}{jk^* r} + \frac{1}{|k|^2 r^2} - \frac{1}{k^2 r^2} + \frac{1}{j|k|^2 k^3} \right)^* \right] \tag{A.5}$$

Substituting

$$\frac{1}{\eta^*} = \frac{c}{\eta_0 \omega} (\beta + j\alpha)$$

Then

$$S_{TE} = \frac{1}{12\pi} (I_m dl |k|)^2 \frac{c}{\eta_0 \omega} e^{-2\alpha r} \beta \left[1 + \frac{2\alpha}{|k|^2 r} \right] \tag{A.6}$$

67